Nonlocal Kondo coupling and selective doping from cerium f electrons in iron-based superconductors

J. Sourd,[1,2] S. Tencé,[2] E. Gaudin,[2] and S. Burdin[1]
[1]*University of Bordeaux, CNRS, LOMA, UMR 5798, F-33400 Talence, France*
[2]*CNRS, University of Bordeaux, Bordeaux INP, ICMCB, UMR 5026, F-33600 Pessac, France*

(Received 24 July 2023; revised 18 December 2023; accepted 21 December 2023; published 9 January 2024)

In this paper, we consider an unconventional doping effect of strongly correlated cerium $4f$ electrons in layered intermetallic systems. The conduction electron part of the model is taken to reproduce the hole and electron pockets of iron-based superconductors (FeSCs), and the cerium contribution is studied through an effective tight-binding Hamiltonian arising from the slave-boson mean-field theory of the periodic Anderson model. We show how the consideration of the nonlocal Kondo coupling naturally present in real materials can lead to a pocket-selective doping effect from cerium f electrons. The model is designed for paramagnetic materials of the ZrCuSiAs-type structure such as CeFeSiH, CeFePO, or the high-pressure phase of CeFeAsO. In certain conditions, the model shows a Lifshitz transition which can be induced by either doping or change in the hybridization strength between iron and cerium orbitals. We present some signatures of both pocket-selective doping and Lifshitz transition by means of the density of states at the Fermi level, the static spin susceptibility, the optical conductivity, and Raman spectroscopy.

DOI: 10.1103/PhysRevB.109.045117

I. INTRODUCTION

Cerium-containing materials represent an active part of the modern research in quantum matter. They display a huge amount of exotic behaviors, such as unconventional superconductivity in $CeCu_2Si_2$ [1], magnetic field-induced quantum critical point in $CeRhIn_5$ [2], non-Fermi liquids [3], or possible quadrupole-density wave in $CeRh_2As_2$ [4], for example.

Out of those very peculiar properties, the heavy-fermion state has gathered an important number of studies. It corresponds to a collective phenomenon where the magnetic moments originating from Ce^{3+} $4f^1$ orbitals form a quantum coherent state with the conduction sea at low temperature, leading to Fermi liquid with strongly renormalized quasiparticles [5,6]. This Fermi liquid state shows an enlarged Fermi surface due to the contribution of cerium $4f^1$ electrons [6], what has been observed in angle-resolved photoemission spectroscopy (ARPES) experiments on CeFePO, for example [7].

On the other hand, the variation of the number of charge carriers is a central point in the study of strongly correlated d-electron materials, and in particular doping induced unconventional superconductivity in the high-T_c cuprates [8] and iron-based superconductors [9].

In this paper, we address the question of the combined effect of f- and d-electron physics in the paramagnetic regime and propose a study of the possible Fermi-surface reconstruction arising from heavy-fermion state in iron-based superconductors of the ZrCuSiAs structure. Some clues for nontrivial cerium f-electron effects have been predicted by dynamical mean-field theory calculations [10] and observed experimentally. For example, CeFePO is a paramagnetic Kondo lattice at low temperature [11], as well as CeFeAsO above 5 GPa [12]. In these two cases, no magnetic order is observed on iron sites. Furthermore, to explain the superconductivity induced with pressure on CeFeAsO, the authors of [12] have pointed out the possible relevance of electron doping from cerium atoms. Another case of interest is the iron-based superconductor LaFeSiH [13], in which no magnetic order on the iron atom has been observed down to low temperatures.

One peculiarity of iron-based superconductors is their multipocket physics at the Fermi level [14]. Interorbital correlations have been shown to explain both magnetic order in the underdoped side and superconductivity as weak coupling instabilities of the d-electron Fermi liquid. The former is a spin density wave arising from the nesting of the electron and hole Fermi surfaces, and for the latter the superconducting $s^{\pm}$ pairing mechanism is associated to interpocket scattering [15]. Thus, through the nesting condition between electron and hole pockets, the shapes and topologies of the Fermi surfaces have a major role in this family of materials.

We will consider the Fermi-surface reconstruction arising from cerium heavy-fermion state by means of a periodic Anderson model. This model has been extensively studied and reproduces heavy-fermion behavior through the apparition of an effective hybridization between the conduction electrons and the cerium orbitals, responsible for Kondo coherence [16,17]. This hybridization creates a pseudogap close to the Fermi energy, or even at the Fermi energy in the case of Kondo insulators. In usual treatments of the periodic Anderson model, only one conduction band and a local hybridization between the conduction electrons and the cerium sites are generally assumed, as for example in [18].

However, in ZrCuSiAs compounds containing iron and cerium, the iron atoms that hold the conduction electrons and the cerium atoms that hold the f orbitals are separated in space. This implies a nonlocal hybridization between the

Bloch electrons and the Kondo ions. This nonlocal hybridization leads to a Kondo gap that varies in the Brillouin zone and, in particular, can show hybridization nodes imposed by symmetry [19].

Momentum-dependent Kondo hybridization is reported experimentally, for example, in optical conductivity [20], in Raman spectroscopy [21], and in ARPES [22–25]. They are also used in theoretical models, for example, to explain the intensity variations observed in the photoemission spectrum of $CePd_3$ [26] or to reproduce optical conductivity measurements performed on $CeTIn_5$ (T = Co, Rh, Ir) [20]. On the periodic Anderson model, it has been shown that the competition between a local hybridization term and a nonlocal hybridization term can lead to unconventional superconductivity mediated by magnetic fluctuations, without inducing *ad hoc* magnetic interactions between cerium atoms [27]. We mention also the case of the Kondo insulators CeRhSb and CeNiSn, where nodes in the Kondo pseudogap are observed in thermal conductivity [28], and are studied theoretically in [29,30].

Following the work of [19], we will consider the possibility of hybridization nodes induced by a nonlocal Kondo coupling. We will extend the method of [19] to a prototype of multiband system for the conduction electrons, adapted for iron-based superconductors physics. We will show how the anisotropic features of the cerium orbitals and of the cerium-iron hybridization can affect the Fermi-surface reconstruction, and the doping through cerium heavy-fermion state. Such model is devoted to paramagnetic systems such as CeFeAsO above 5 GPa or CeFePO in which doping effect of cerium has been observed [7,12], or to CeFeSiH, the heavy-fermion cerium compound associated to the iron-based superconductor LaFeSiH [13].

In the first section, we present the tight-binding model adapted for FeSCs physics at low energy and the slave-boson method we used to treat the strong correlations of the cerium f orbitals. In the second section, we present the results on the electronic structure, and propose some physical observables for the pocket-selective doping effect. Finally, we discuss the results considering the existing measurements on materials that might undergo a related behavior.

II. MODEL AND METHOD

A. Model and slave-boson approach

This work is motivated by the ZrCuSiAs family of FeSCs such as LaFeAsO, LaFePO, and LaFeSiH, and in particular their cerium counterparts CeFeAsO, CeFePO, and CeFeSiH. We will thus focus on one iron plane surrounded by cerium atoms, presented in Fig. 1. The unit cell contains two iron and two cerium atoms because of the alternated positions of cerium atoms with respect to the iron plane.

The two iron atoms' unit cell has been shown to be an important ingredient of the electronic structure of FeSCs, in particular due to the presence of spin-orbit coupling for the iron d orbitals [31]. However, in order to investigate more precisely the pocket-selective doping of cerium f electrons, we will consider the simpler model of a unit cell with only one iron atom. This approximation preserves the principal aspect

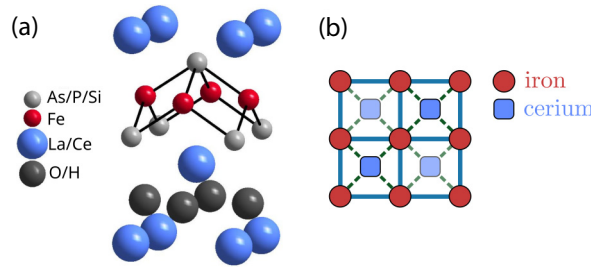

FIG. 1. (a) Crystal structure of LaFeAsO, LaFePO, LaFeSiH, CeFeAsO, CeFePO, and CeFeSiH, representing the ZrCuSiAs family of FeSCs. (b) Square lattice of the iron plane. The alternated (above and under) blue squares represent the cerium positions with respect to the iron square lattice.

of the electronic structure for the iron d electrons which is the multipocket physics at the Fermi level. Furthermore, it permits a simpler understanding of the pocket-selective doping due to a smaller number of electronic bands.

In order to separate the d-electron physics from the f-electron physics, we will also consider LaFeSiH, which is isostructural to CeFeSiH and without any f electron.

The Hamiltonian contains the effects of iron d electrons, cerium f electrons, and a fd hybridization term. It is written as

$$\mathcal{H} = \mathcal{H}_d + \mathcal{H}_f + \mathcal{H}_{fd}. \tag{1}$$

The precise content of each term will be described hereafter.

1. *d*-electron physics $\mathcal{H}_d$

For the d-electron physics, we take the two-band model of Raghu *et al.* [32], represented in Fig. 2. This model consists of the two iron d^{xz} and d^{yz} orbitals, and the associated hopping parameters are shown in Fig. 2(a).

Denoting $d^{\alpha}_{k\sigma}$ as the destruction of an iron d electron of orbital index $\alpha = xz, yz$, spin $\sigma = \uparrow, \downarrow$, and momentum k, the d-electron Hamiltonian is written as

$$\mathcal{H}_d = \sum_{k\sigma\alpha\alpha'} \left(\epsilon_k^{\alpha\alpha'} - \mu\delta^{\alpha\alpha'}\right) d^{\alpha\dagger}_{k\sigma} d^{\alpha'}_{k\sigma}. \tag{2}$$

We write N the number of iron sites, equal to the number of cerium sites. The creation operators in real space are written as $d^{\alpha}_{i\sigma} = \frac{1}{\sqrt{N}} \sum_k d^{\alpha}_{k\sigma} e^{i\mathbf{k}\cdot\mathbf{r}_i}$, and the energies $\epsilon_k^{\alpha\alpha'}$ are obtained as the Fourier transform of the hopping parameters $t_{ij}^{\alpha\alpha'}$ defined in Fig. 2(a), $\epsilon_k^{\alpha\alpha'} = \sum_{ij} e^{i\mathbf{k}\cdot(\mathbf{r}_i - \mathbf{r}_j)} t_{ij}^{\alpha\alpha'}$:

$$\begin{aligned}
\epsilon_k^{xx} &= -2t_1\cos(k_x) - 2t_2\cos(k_y) - 4t_3\cos(k_x)\cos(k_y),\\
\epsilon_k^{yy} &= -2t_1\cos(k_y) - 2t_2\cos(k_x) - 4t_3\cos(k_x)\cos(k_y),\\
\epsilon_k^{xy} &= 4t_4\sin(k_x)\sin(k_y).
\end{aligned} \tag{3}$$

The chemical potential term μ permits to vary the number of conduction electrons n_d.

2. *f*-electron physics $\mathcal{H}_f$

For the cerium $4f^1$ physics, we focus on the low-energy Kramers doublet resulting from spin-orbit and crystal-field splittings, and responsible for Kondo effect. While it has been possible to neglect spin-orbit coupling for the iron $3d$ orbitals

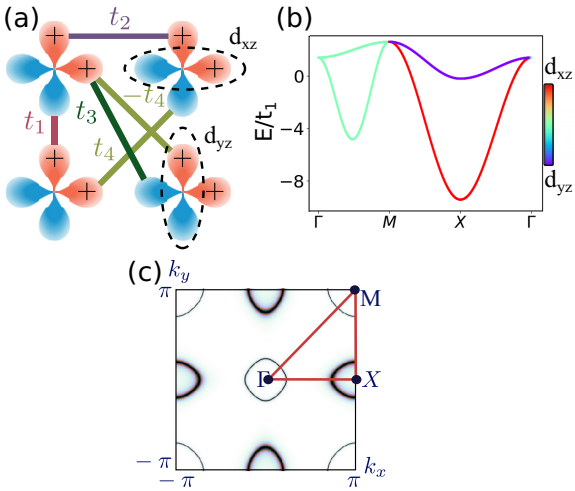

FIG. 2. (a) Tight-binding model of Ref. [32]. (b) Band structure on the high-symmetry path of the Brillouin zone. E is the energy of the two conduction bands defined by $2E_{\pm}(k) = \epsilon_k^{xx} + \epsilon_k^{yy} - 2\mu \pm \sqrt{(\epsilon_k^{xx} - \epsilon_k^{yy})^2 + 4(\epsilon_k^{xy})^2}$. The content of d^{xz} or d^{yz} electrons in each band is represented in color from violet to red. (c) Associated Fermi surfaces, typical of iron-based superconductors. The two hole pockets are located around Γ and M, and the two electron pockets are located around X and its second equivalent position. The solid red line indicates the high-symmetry path $\Gamma \to M \to X \to \Gamma$.

and preserve the multiband structure at the Fermi level, such spin-orbit interaction cannot be neglected for the cerium $4f$ orbitals. Considering only the low-energy Kramers doublet, we are indeed in the opposite regime, in which the spin-orbit coupling is much larger than the other energy scales of the system. This is justified since spin-orbit coupling is much more important for $4f$ orbitals than $3d$ orbitals.

In a tetragonal system such as FeSCs, the Kramers doublet arising from $J = \frac{5}{2}$ low-energy spin-orbit multiplet is either Γ_6, Γ_7^+, or Γ_7^- depending on the ionic environment [33]. Their symmetry properties with respect to square plane group transformations are represented in Fig. 3.

We will consider the three cases of Γ_6, Γ_{7+}, or Γ_{7-} separately. The localized low-energy doublet is represented through an atomic level of energy ϵ_f, with Hubbard repulsion U, denoting $f_{\delta\sigma}$ the destruction of a cerium f electron of

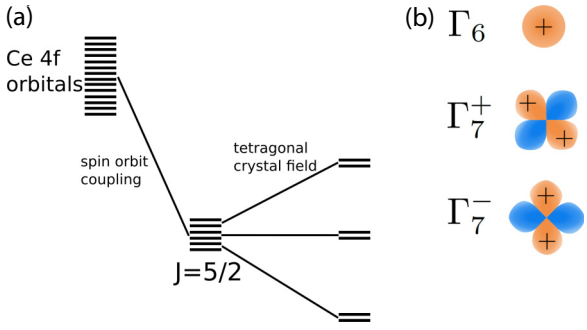

FIG. 3. (a) Spin-orbit and crystal-field splittings of the cerium $4f$ orbital in the tetragonal environment. (b) Symmetry properties under square plane group operations D^4 for the low-energy doublets Γ_6, Γ_{7+}, and Γ_{7-}.

pseudospin $\sigma = \uparrow, \downarrow$ at site δ:

$$\mathcal{H}_f = \epsilon_f \sum_{\delta\sigma} f_{\delta\sigma}^\dagger f_{\delta\sigma} + U \sum_{\delta} f_{\delta\uparrow}^\dagger f_{\delta\uparrow} f_{\delta\downarrow}^\dagger f_{\delta\downarrow}. \tag{4}$$

We assume a strong Coulomb repulsion on the f orbital which corresponds to the limit $U \to \infty$. In order to look at the low-energy physics and discard the high-energy part of the Hilbert space where there are two electrons on at least one cerium site, we use the slave-boson technique [16,34–36]. It permits to avoid the interaction term U, at the price of replacing the fermionic operator by a composite one $f_{\delta\sigma} \to b_\delta^\dagger \tilde{f}_{\delta\sigma}$ where b_δ and $\tilde{f}_{\delta\sigma}$ annihilate, respectively, an auxiliary boson and fermion. This transformation is valid with the local constraint on each site to ensure the closure of the Hilbert space: $\sum_\sigma \tilde{f}_{\delta\sigma}^\dagger \tilde{f}_{\delta\sigma} + b_\delta^\dagger b_\delta = 1$.

Here, the physical doublet states $4f^1$ are identified with $\tilde{f}_{\delta\sigma}^\dagger |\tilde{0}\rangle_\delta$, where $|\tilde{0}\rangle_\delta$ denotes an auxiliary vacuum. The $4f^0$ state is identified with $b_\delta^\dagger |\tilde{0}\rangle_\delta$. Since the boson-number operator $b_\delta^\dagger b_\delta$ is always positive, states for which $\sum_\sigma \tilde{f}_{\delta\sigma}^\dagger \tilde{f}_{\delta\sigma} > 1$ are automatically forbidden on each site, and then the explicit interaction term U in Eq. (4) can be suppressed. The constraint is achieved through the introduction of a local Lagrange multiplier λ_δ, which has to be fixed self-consistently. Thanks to the operator identity $f_{\delta\sigma}^\dagger f_{\delta\sigma} = \tilde{f}_{\delta\sigma}^\dagger \tilde{f}_{\delta\sigma}$, the Hamiltonian for f electrons is mapped onto

$$\mathcal{H}_f \to \epsilon_f \sum_{\delta\sigma} \tilde{f}_{\delta\sigma}^\dagger \tilde{f}_{\delta\sigma} + \sum_\delta \lambda_\delta \left(\sum_\sigma \tilde{f}_{\delta\sigma}^\dagger \tilde{f}_{\delta\sigma} + b_\delta^\dagger b_\delta - 1 \right). \tag{5}$$

3. *fd hybridization* $\mathcal{H}_{fd}$

Given the crystal structure of CeFeAsO, CeFePO, or CeFeSiH represented in Fig. 1(b), one can formally write the hybridization between cerium f orbital at site δ and iron d^α orbitals at site i as

$$\mathcal{H}_{fd} = v \sum_{i\delta\alpha\sigma} \left(\gamma_{i\delta}^\alpha f_{\delta\sigma}^\dagger d_{i\sigma}^\alpha + \text{H.c.} \right). \tag{6}$$

The sign of the structure factor $\gamma_{i\delta}^\alpha$ depends on the symmetry of the low-energy cerium Kramers doublet Γ_6, Γ_7^+, or Γ_7^-, as represented in Fig. 4. Using Fourier transform $\gamma_k^\alpha = \sum_{i\delta} e^{ik(r_i - r_\delta)} \gamma_{i\delta}^\alpha$, we have

$$\begin{aligned}
\Gamma_6 &: \gamma_k^x = -4i \sin\frac{k_x}{2}\cos\frac{k_y}{2}, \quad \gamma_k^y = -4i \sin\frac{k_y}{2}\cos\frac{k_x}{2}, \\
\Gamma_{7+} &: \gamma_k^x = 4i \sin\frac{k_x}{2}\cos\frac{k_x}{2}, \quad \gamma_k^y = 4i \sin\frac{k_x}{2}\cos\frac{k_y}{2}, \\
\Gamma_{7-} &: \gamma_k^x = -4i \sin\frac{k_x}{2}\cos\frac{k_y}{2}, \quad \gamma_k^y = 4i \sin\frac{k_y}{2}\cos\frac{k_x}{2}.
\end{aligned} \tag{7}$$

In this model, we assume the same magnitude for the hybridization v between the cerium and the two iron orbitals. This is required by symmetry since the isolated d^{xz} or d^{yz} do not form a representation of the square plane group alone, but constitute a doublet $\{d^{xz}, d^{yz}\}$.

After the slave-boson mapping, the hybridization term becomes

$$\mathcal{H}_{fd} \to v \sum_{i\delta\alpha\sigma} \left(\gamma_{i\delta}^\alpha b_\delta \tilde{f}_{\delta\sigma}^\dagger d_{i\sigma}^\alpha + \text{H.c.} \right), \tag{8}$$

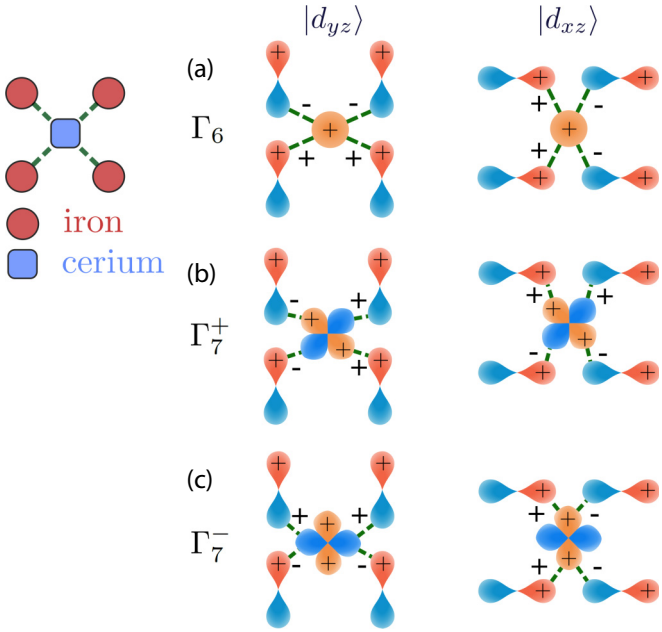

FIG. 4. Nearest-neighbor hybridization between the f orbital of cerium and the d^{yz} and d^{xz} orbitals of iron, for the Γ_6 symmetry (a), Γ_{7+} symmetry (b), or Γ_{7-} symmetry (c).

where the hybridization strength between d electrons and $\tilde{f}$ pseudofermions has been dressed by the slave-boson field b_δ.

B. Mean-field approximation

We perform a static and homogeneous mean-field approximation on both boson field b and Lagrange multiplier λ. Using Eqs. (2), (5), and (8) for $\mathcal{H}_d$, $\mathcal{H}_f$, and $\mathcal{H}_{fd}$, we get an effective tight-binding model, written in k space:

$$\begin{aligned}\mathcal{H} &= \mathcal{H}_d + \mathcal{H}_f + \mathcal{H}_{fd} \\ &\approx \sum_{k\sigma\alpha\alpha'} \left(\epsilon_k^{\alpha\alpha'} - \mu\delta_{\alpha\alpha'}\right) d_{k\sigma}^{\alpha\dagger} d_{k\sigma}^{\alpha'} + (\lambda-\mu)\sum_{k\sigma} \tilde{f}_{k\sigma}^\dagger \tilde{f}_{k\sigma} \\ &\quad + vb\sum_{k\sigma\alpha}\left(\gamma_k^\alpha \tilde{f}_{k\sigma}^\dagger d_{k\sigma}^\alpha + \text{H.c.}\right) + \epsilon_0, \\ \epsilon_0 &= N(\lambda-\epsilon_f)(b^2-1) + N\mu(1-b^2+n_d). \end{aligned} \tag{9}$$

Following the standard slave-boson mean-field procedure, the mean-field parameters are fixed from the saddle-point equations of the free energy $\mathcal{F} = -\frac{1}{\beta}\exp(-\beta\mathcal{H})$ with respect to b, λ, and μ:

$$\begin{aligned} &\frac{v}{N}\sum_{k\sigma\alpha}\gamma_k^\alpha\left\langle\left(\tilde{f}_{k\sigma}^\dagger d_{k\sigma}^\alpha + \text{H.c.}\right)\right\rangle + 2b(\lambda-\mu-\epsilon_f) = 0, \\ &\frac{1}{N}\sum_{k\sigma}\left\langle\tilde{f}_{k\sigma}^\dagger \tilde{f}_{k\sigma}\right\rangle + b^2 - 1 = 0, \\ &\frac{1}{N}\sum_{k\sigma\alpha}\left\langle d_{k\sigma}^{\alpha\dagger} d_{k\sigma}^\alpha\right\rangle + \frac{1}{N}\sum_{k\sigma}\left\langle\tilde{f}_{k\sigma}^\dagger \tilde{f}_{k\sigma}\right\rangle + b^2 - 1 - n_d = 0, \end{aligned} \tag{10}$$

where $\langle\dots\rangle$ denotes thermodynamical average with respect to $\mathcal{H}$. For the following, we write the mean-field Hamiltonian (9) as

$$\begin{aligned}\mathcal{H} &\approx \sum_{k\sigma}\left(d_{k\sigma}^{x\dagger}, d_{k\sigma}^{y\dagger}, \tilde{f}_{k\sigma}^\dagger\right) M_k \begin{pmatrix} d_{k\sigma}^x \\ d_{k\sigma}^y \\ \tilde{f}_{k\sigma} \end{pmatrix} + \epsilon_0, \\ M_k &= \begin{pmatrix} \epsilon_k^{xx}-\mu & \epsilon_k^{xy} & vb\gamma_k^x \\ \epsilon_k^{xy}-\mu & \epsilon_k^{yy}-\mu & vb\gamma_k^y \\ \left(vb\gamma_k^x\right)^* & \left(vb\gamma_k^y\right)^* & \lambda-\mu \end{pmatrix}. \end{aligned} \tag{11}$$

For fixed d-electron band-structure parameters $\epsilon_k^{\alpha\alpha'}$ and filling n_d, the model displays two free parameters: the number of doping f electrons $n_f = \frac{2}{N}\sum_k\langle\tilde{f}_{k\sigma}^\dagger\tilde{f}_{k\sigma}\rangle$, and the strength of the effective hybridization vb.

The mean-field equations (10) have a trivial solution $b = 0$, which is realized at high temperature. It corresponds to decoupled d and f electrons. A second solution $b \neq 0$ can be realized under a typical temperature T_K called the Kondo temperature. Below T_K, the appearance of an effective hybridization between $\tilde{f}$ pseudofermions and d electrons is associated with the Fermi-surface reconstruction and the doping effect of cerium.

Within the phenomenological model presented here, we will study the physics of the ground state at $T = 0$. In order to adapt qualitatively our discussion to real materials, we define an energy scale

$$T_0 = (4vb)^2/W, \tag{12}$$

where $W \approx 12|t_1|$ is the bandwidth for the conduction electrons. In usual slave-boson treatments of the Kondo lattice with local fd hybridization, we may identify $T_0 \approx T_K$. The cases where $T_0 \ll T_K$ or $T_0 \gg T_K$ that might be realized in some specific situations [35,37] are not discussed here. We suppose for this work that the relation $T_0 \approx T_K$ is still valid in the nonlocal fd hybridization case.

III. RESULTS AND DISCUSSION

For the numerical calculations, we fix the energy scale of the model $|t_1|$ from ARPES experiments in FeSCs [38] which shows that the bandwidth of the hole pocket centered at Γ (that consists of iron d^{xz} and d^{yz} orbitals) has a depth around 150 meV. The top of the hole band at Γ is around $2|t_1|$, which gives $|t_1| = 825$ K, and $W = 12|t_1| \approx 9900$ K. Thus, we take as lowest hybridization $vb = 0.2|t_1|$ that corresponds to $T_0 \approx 4(vb)^2/W \approx 10$ K. This is typical for those systems, e.g., CeFePO [11] or CeFeAsO at 5 GPa [12].

Thus, given an undoped band structure, an amount of doping f electrons and a given Kondo temperature, the model is fixed. The control parameter can be either the number of f electrons n_f at fixed fd hybridization vb, or the fd hybridization vb at fixed number of f electrons n_f. Varying n_f can be viewed as tuning the cerium concentration x in a $La_{1-x}Ce_xFeSiH$ system, for example, assuming that x is not too small such that the cerium $4f$ electrons contribute to the coherent Fermi-liquid state [39,40]. We suppose for this work that the Kondo coherent state is achieved even at small number of f electrons n_f. Varying the fd hybridization strength vb corresponds to the increase of overlap between the cerium

orbital and the conduction electrons, which can be achieved through the application of external pressure.

A. Electronic structure

In this section, we analyze the band structure, the Fermi-surface reconstruction, as well as the density of states at the Fermi level for different symmetries for the low-energy cerium orbital.

1. Band crossing

The principal effect induced by the nonlocal fd hybridization in real space is k-dependent hybridization in reciprocal space and in particular hybridization nodes. To represent this result, we fix the number of f electrons $n_f = 0.2$ and take $vb = 0.2|t_1|$. The results are shown in Fig. 5.

We obtain different results depending on the cerium orbital symmetry. In the case of Γ_6 cerium, the f band hybridizes with the lower d band around Γ and M which corresponds to the hole pockets (the gap is denoted Δ_1), and not with the upper d band around X, which corresponds to the electron pockets [see Fig. 5(a)]. For the Γ_{7+} cerium, the situation is reversed and the f level does not hybridize with the lower band in $M \to X \to \Gamma$ and hybridize with the upper band in this region (the gap is denoted Δ_2) [see Fig. 5(b)]. In this case, the hybridization gap Δ_1 that is visible in $\Gamma \to M$ lies too much above the Fermi level in this case to generate a Fermi-surface reconstruction. Finally in the case of Γ_{7-}, the cerium f band does not hybridize nor with the lower band in $\Gamma \to M$, nor with the upper band in $M \to X \to \Gamma$ [see Fig. 5(c)].

In this last case of symmetry Γ_{7-}, the cerium $4f$ band does not hybridize enough with the iron d^{xz} and d^{yz} bands, and the added f electrons create a new pocket in the path $\Gamma \to M$, which is quite artificial [see Fig. 5(c)]. However, different results might be obtained considering iron d^{xy} and d^{z^2} bands, which are not considered here. All the allowed or forbidden crossings can be obtained directly from symmetry considerations on the band structure (see Appendix A).

2. Variation of f-electron number and pocket-selective doping

The study of the band crossing showed that we can discard the case Γ_{7-} cerium in the following since it does not lead to a strong enough fd hybridization. We analyze the Fermi-surface reconstruction upon adding f electrons to the system. The Fermi surfaces correspond to the solutions of the equation $E_k^\nu = 0$, $\nu = 1, 2, 3$, where E_k^ν are the eigenvalues of the matrix M_k defined in Eq. (11).

In the case of Γ_6 cerium [see Fig. 6(a)], the added electrons fill the hole pockets, in agreement with the results of band crossing. For $vb/|t_1| = 0.2$, the complete filling of the hole pockets leads to their extinction around $n_f = 0.3$, what constitutes a Lifshitz transition [41]. Continuing to add f electrons to the system, they populate the electron pockets until a second Lifshitz transition occurs at $n_f = 0.5$, where the two electron pockets merge and form two hole pockets centered at Γ and M.

In the case of Γ_{7+} cerium symmetry [see Fig. 6(b)], the added electrons populate almost only the electron pockets in accordance with the results of the previous section [see Fig. 5(b)]. For $vb/|t_1| = 0.2$, no Lifshitz transition is observed up to $n_f = 1$.

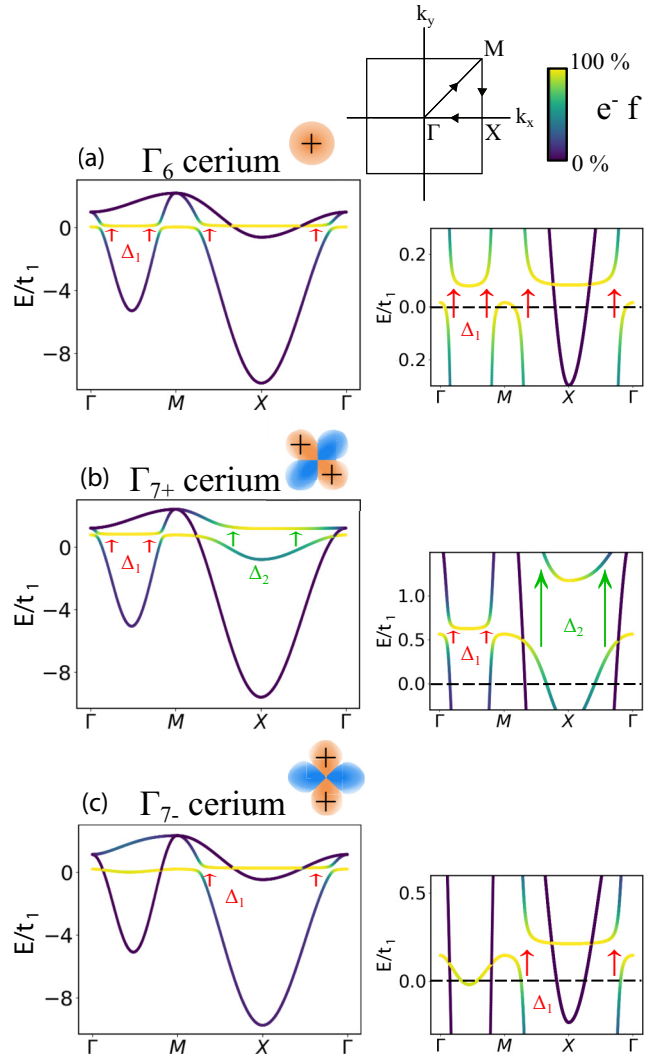

FIG. 5. Band structure corresponding to the eigenvalues of the matrix M_k defined in Eq. (11), on the high-symmetry contour $\Gamma \to M \to X \to \Gamma$, in the case of Γ_6 cerium (a), Γ_{7+} cerium (b), and Γ_{7-} cerium (c), for $n_f = 0.2$ and $vb = 0.2|t_1|$. The proportion of f electrons in each band is represented in color from dark blue to yellow. Δ_1 refers to the hybridization gap between the cerium f band and the lower d band, whereas Δ_2 refers to the hybridization gap between the cerium f band and the upper d band.

Thus, the model predicts that depending on the cerium orbital symmetry, the added f electrons will populate either the hole or the electron pockets in priority, what we refer as the pocket-selective doping of cerium f electrons in iron-based superconductors.

We can discuss the pocket-selective doping in the framework of ARPES experiments in CeFePO [7] and CeRuPO [42], and by comparing with their lanthanum-based counterparts that will correspond to the $n_f = 0$ case of this model. In CeFePO, the two hole pockets around Γ are observed to be smaller than the one of LaFePO [7]. We thus expect that these hole pockets are partially filled by the cerium f electrons, which correspond to the Γ_6 cerium case of this model.

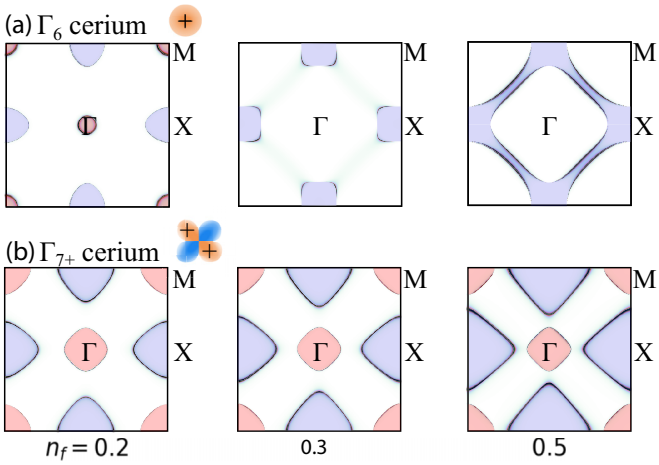

FIG. 6. Evolution of Fermi surfaces upon adding f electrons to the system for $vb/|t_1| = 0.2$, in the case of Γ_6 cerium symmetry (a), and Γ_{7+} cerium symmetry (b). For more clarity, electron pockets are represented in blue, and hole pockets are represented in red. Two Lifshitz transitions are observed for the Γ_6 cerium at $n_f = 0.3$ and 0.5.

Furthermore, a hybridization with the $d^{z^2-r^2}$ band is observed, that we did not consider here. CeRuPO is known to be a ferromagnetic Kondo lattice compared to the paramagnetic compound CeFePO. Nevertheless, the same hybridization with the d^{xz}, d^{yz}, and $d^{z^2-r^2}$ bands has been reported [42]. Apart from the case of the $d^{z^2-r^2}$ orbital, the model presented here agrees with the Γ_6 cerium ground state observed in CeRuPO from magnetic susceptibility measurements on single crystals [43].

Finally, we expect that these results could extend to paramagnetic heavy-fermion regime induced above 5 GPa in CeFeAsO [12], where the possible doping from cerium atoms has been pointed out. Magnetic susceptibility measurements on CeFeAsO single crystals indicate a Γ_6 cerium ground state [44]. The model presented here predicts that this Γ_6 doublet leads to doping of the hole pockets. In order to describe the low-pressure phase of CeFeAsO, one should take into account both magnetic order on the cerium atom, and also magnetic order on the iron atom like in [45], which is beyond the scope of the present discussion.

3. *The Lifshitz transition of* Γ_6 *cerium*

Among the two Lifshitz transitions identified in the previous section, we will now study in detail only the one corresponding to the complete filling of the hole pockets. The associated Fermi surfaces are represented in Fig. 7(a) for different values of the hybridization strength vb. We first remark that in all cases both hole pockets disappear at the same time. This can be understood by observing that the fd structure factors γ_k^x and γ_k^y are equal to zero at the Γ and M points [see Fig. 5(a)]. Thus, the disappearance of the hole pockets corresponds to the crossing of the f level through the Fermi energy, which occur at the same time for both hole pockets and corresponds to our model parameters $\lambda - \mu = 0$ [see Fig. 7(b)].

This transition is strongly affected by the fd hybridization strength vb, contrary to the case of Γ_{7+} cerium where the

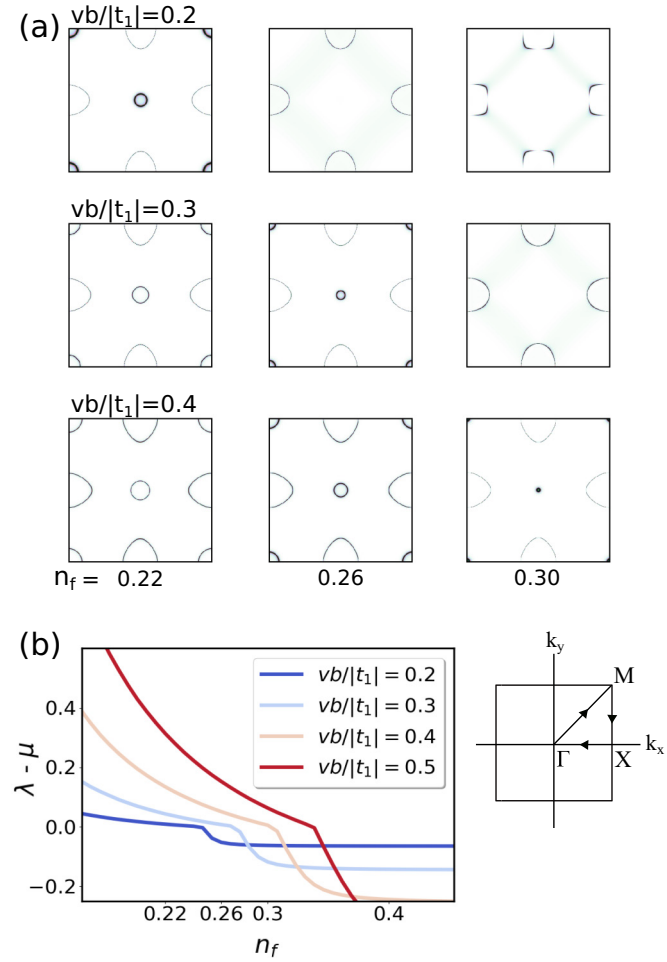

FIG. 7. (a) Lifshitz transition of Γ_6 cerium where the hole pockets disappear, for different hybridization strength vb. (b) Lifshitz transition of Γ_6 cerium identified as the crossing of the flat level through the Fermi energy $\lambda - \mu = 0$.

reconstruction of Fermi surfaces is independent of vb (not shown). The hole pockets disappear towards higher doping as the fd hybridization strength vb increases. This can be explained as follows: the self-consistency equations (10) fix λ and μ in order to satisfy the physical constraints of the number of d electrons per site n_d and the total number of electrons per site $n_d + n_f$. When $\lambda - \mu > 0$, in order to increase vb at fixed $n_d + n_f$, one has to put the effective f level higher in energy, and increase λ. However, as there is a mixing between the f and the d bands, a higher f band also implies less d electrons. So one has to correct this also by increasing μ. Since there is no hybridization between the f band and the electron pockets, these two combined effects lead to a transfer of d electrons from the hole pockets to the electron pockets. Finally, since there are fewer electrons occupying the hole pockets, a larger number of f electrons are needed to reach the complete filling.

Also, let us notice that at the precise point of the transition, there is no more contribution of the f electrons to the Fermi surfaces, which then contain only the "light" electrons.

We are aware that the multiorbital interactions in the d manifold should also have a role [46,47]. However, here, we neglect their effect and we use a slave-boson mean field that

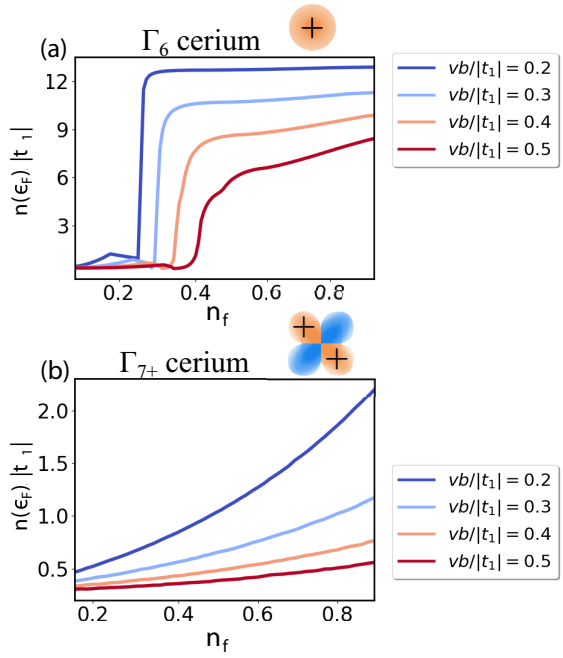

FIG. 8. Density of states at the Fermi level $n(\epsilon_F)$ variation versus the hybridization strength vb at different number of doping f electrons n_f, for Γ_6 cerium (a) and Γ_{7+} cerium symmetry (b).

focuses onto the f-electron interaction. This minimal content permits to focus on the pocket-selective doping effect of cerium more transparently.

4. Density of states at the Fermi level

The density of states at the Fermi level is a central quantity to discuss heavy-fermion behavior. In a Fermi-liquid picture of a given material, it corresponds to the effective mass of the quasiparticles and can directly be probed through several measurements: specific heat, electrical resistivity, thermopower coefficient, and static spin susceptibility [48,49].

For a multiband system of band index $\nu = 1, 2, 3$ and energies E_k^ν defined as the eigenvalues of the matrix M_k, the total density of states at the Fermi level is expressed as the sum over the band index: $n(\omega + \epsilon_F) = \sum_{k\nu} \delta(\omega - E_k^\nu)$, where ϵ_F is the Fermi energy. In Fig. 8 we show the evolution of the density of states at the Fermi level for the Γ_6 and Γ_{7+} cerium, varying the numbers of doping f electrons n_f, for different fd hybridization strength vb.

For Γ_6 cerium [see Fig. 8(a)], we observe a very strong increase of the density of states at the Fermi level. Moreover, the evolution of this density of states as a function of the number of f electrons or hybridization is not smooth, and shows a singular behavior at the first Lifshitz transition, where the hole pockets are completely filled. As we noticed when studying the reconstruction of the Fermi surfaces, at the transition point the f electrons no longer contribute to the conduction, and thus the density of states at the Fermi level reaches a local minimum.

For Γ_{7+} cerium [see Fig. 8(b)], the density of states at the Fermi level increases smoothly with the number of f electrons n_f, and decreases smoothly with the hybridization vb. This result is consistent with the reconstruction of the Fermi surfaces which is independent of the vb hybridization.

While a quantitative prediction of the effective mass for a given material is beyond the scope of this paper, we expect qualitative signatures depending on the cerium orbital symmetry. In particular, we remark a qualitative agreement with CeFePO, at least in order of magnitude. For a Γ_6 cerium with $vb/t_1 = 0.2$, corresponding to a Kondo temperature $T_0 \approx T_K \approx 10$ K, we obtain an increase of the density of states at the Fermi level by a factor 37. In CeFePO, the Kondo temperature has been estimated from the entropy to $T_K \approx 10$ K [11], and comparing the Sommerfeld coefficient $\gamma_{\text{CeFePO}} = 700$ mJ/mol K^2 to the one of LaFePO $\gamma_{\text{LaFePO}} = 12.5$ mJ/mol K^2 [50], we obtain a factor 56.

B. Physical observables

In this section, we propose additional observables to distinguish signatures of the different symmetries for the cerium orbital. We will first study the static spin susceptibility, which can be compared with the density of states at the Fermi level determined in the previous section. Second, we will study the optical conductivity and the Raman spectra, which will be discussed with the help of the results obtained for the band crossing.

1. Static spin susceptibility

In FeSCs, it is generally assumed that the nesting between the hole pocket at the center of the Brillouin zone and the electron pockets at the edge leads to enhanced $(0, \pi)$ magnetic response that tends to destabilize the Fermi liquid in favor to either spin density wave state or $s^\pm$ superconductivity [51,52]. Those $(0, \pi)$ fluctuations arise naturally in the static spin susceptibility. Thus, we expect that the Fermi-surface reconstruction should be associated with changes in nesting conditions and might be visible on static spin susceptibility.

Writing the spin operators as $S_i^{a+} = c_{i\uparrow}^{a\dagger} c_{i\downarrow}^a$, $S_i^{a-} = c_{i\downarrow}^{a\dagger} c_{i\uparrow}^a$, $a = x, y, f$, with $c_{i\uparrow}^x = d_{i\uparrow}^{xz}$, $c_{i\uparrow}^y = d_{i\uparrow}^{yz}$, and $c_{\delta\uparrow}^f = \tilde{f}_{\delta\uparrow}$, the spin susceptibility as a function of imaginary time τ can be expressed as a spin-spin correlation function:

$$\chi_{ij}(\tau) = \sum_{aa'} \left\langle S_j^{a+}(\tau) S_i^{a'-}(0) \right\rangle, \tag{13}$$

where $\langle \dots \rangle$ stands for thermodynamical average. Within the slave-boson mean-field approximation, the effective dressed electrons are noninteracting and the susceptibility can be replaced by a Lindhard-type term:

$$\chi_{ij}(\tau) = -\sum_{aa'} G_{ij}^{a'a}(\tau) G_{ji}^{aa'}(-\tau), \tag{14}$$

where $G_{ij}^{a'a}(\tau) = \langle \mathcal{T}_\tau c_{j\uparrow}^a(\tau) c_{i\uparrow}^{a'\dagger}(0) \rangle = \langle \mathcal{T}_\tau c_{j\downarrow}^a(\tau) c_{i\downarrow}^{a'\dagger}(0) \rangle$ is the Green's function, and $\mathcal{T}_\tau$, the chronological order operator. After Fourier transform, the spin susceptibility $\chi(q, i\Omega)$ is obtained in the reciprocal space k, q and with the Matsubara frequencies $i\omega_n$:

$$\chi(q, i\Omega) = -\frac{1}{\beta N} \sum_{k, i\omega_n aa'} G^{a'a}(k + q, i\omega_n + i\Omega) G^{aa'}(k, i\omega_n). \tag{15}$$

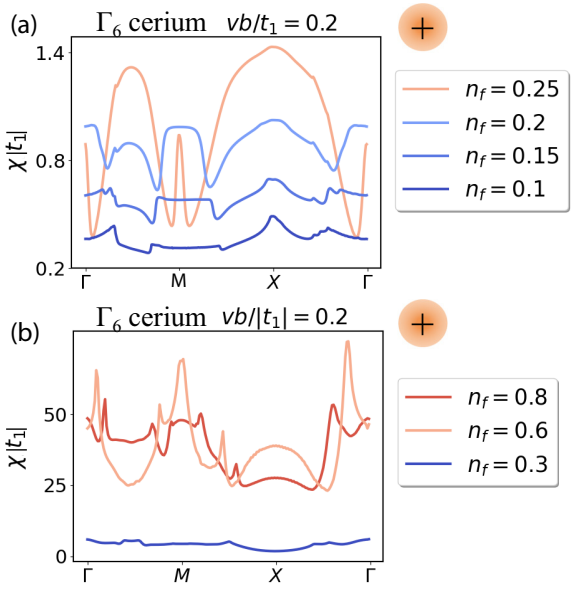

FIG. 9. Static spin susceptibility for Γ_6 cerium with different n_f and $vb/|t_1| = 0.2$.

We will study here the static response $\chi(q) = \chi(q, i\Omega = 0)$. While in [32] or [53] the $T \to 0$ limit is taken by calculating the sum over the $i\omega$ with the residue theorem, we had to adopt here a different strategy. Indeed, the description of an effective f level that crosses the Fermi level required us to sample the Brillouin zone very finely to avoid numerical noise (at least 512×512 close to the Lifshitz transition at $vb/|t_1| = 0.2$ and $n_f = 0.25$), which makes it impossible to perform a sum over four loops with 512^4 points to probe k and $k + q$. Instead, we used the convolution properties of $\chi(q)$ to use the fast Fourier transform (FFT), and then perform the sum over the Matsubara frequencies. This procedure allows us to avoid numerical noise in a controlled way, by progressively increasing the number of Matsubara frequencies, which is equivalent to progressively lowering the temperature. We went up to a maximum of 500 000 Matsubara frequencies with an energy cutoff at twice the bandwidth $2W \approx 25|t_1|$, which gives us results at a temperature of $T \approx 10^{-4}|t_1| \approx 10^{-3}vb$, of the order of 0.1 K.

The results can be understood as arising from two contributions: a constant contribution coming from the density of states at the Fermi level $n(\epsilon_F) \propto \chi(\Gamma)$, and a k-dependent modulation that depends on the nesting conditions between the different pockets.

For Γ_6 cerium we have two regimes. For $n_f < 0.2$ [see Fig. 9(a)], the static spin susceptibility shows an increase in the constant contribution and the formation of a peak at the M point, which corresponds to the nesting between the hole pockets. Moreover, we observe a decrease of $\chi(\Gamma)$ between $n_f = 0.2$ and 0.25, in agreement with the decrease of density of states at the Fermi level [see Fig. 8(a)]. In contrast, at $n_f > 0.25$ [see Fig. 9(b)], the contribution $\chi(\Gamma)$ to the spin susceptibility saturates and only the modulation in the Brillouin zone corresponding to the nesting varies, in agreement with the density of states at the Fermi level which is approximately constant [see Fig. 8(b)].

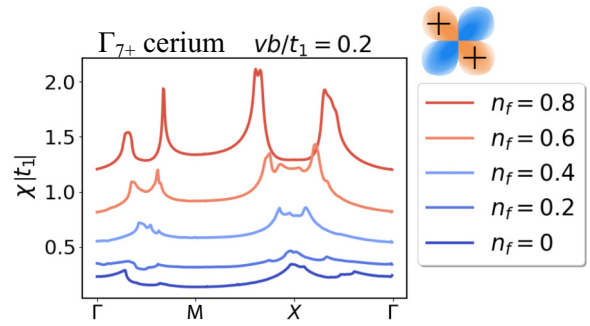

FIG. 10. Static spin susceptibility for Γ_{7+} cerium with different n_f and $vb/|t_1| = 0.2$.

For Γ_{7+} cerium (see Fig. 10), we observe a small increase in the constant contribution, in agreement with the increase in density of states at the Fermi level. At $n_f = 0$, the peak at the X point is associated with $(0, \pi)$ fluctuations of iron-based superconductors. This peak splits into two distinct contributions, which is associated with the growing size difference between the electron and hole pockets.

Thus, the presented model presents several features. First, the peak at the X point associated to the $(0, \pi)$ fluctuations typical of iron-based superconductors disappears in both cases, indicating a lower nesting between the holes and the electrons pockets due to cerium doping. Associated to this effect, we observe a general increase of the spin susceptibility upon adding f electrons, corresponding to the heavy-fermion behavior. Furthermore, the susceptibility profile in momentum space is different between the two cerium symmetries, for example, with the peak at the M point indicating (π, π) fluctuations in the case of the Γ_6 cerium, which is absent in the case of Γ_{7+} cerium. This effect corresponds to the difference of the Fermi-surface reconstruction.

2. *Optical conductivity*

Optical conductivity measurements are very useful to characterize heavy-fermion compounds. They permit a direct identification of the Kondo pseudogap vb, and also the density of states at the Fermi level [54]. Using the compact notation with $c^x_{k\sigma} = d^{xz}_{k\sigma}$, $c^y_{k\sigma} = d^{yz}_{k\sigma}$, and $c^f_{k\sigma} = \tilde{f}_{k\sigma}$, the Hamiltonian (9) is written as

$$\mathcal{H} = \sum_{kaa'\sigma} \epsilon^{aa'}_k c^{a\dagger}_{k\sigma} c^{a'}_{k\sigma} + \epsilon_0 = \sum_{k\nu\sigma} E^\nu_k c^{\nu\dagger}_{k\sigma} c^\nu_{k\sigma} + \epsilon_0. \tag{16}$$

From the calculation available in Appendix B, the real part of the optical conductivity $\sigma(\omega) = \sigma'(\omega) + i\sigma''(\omega)$ at $T = 0$ is written as

$$\sigma'^{xx}(\omega) = \mathrm{Re}\left\{ \frac{2i}{\omega + i\Gamma_{el}} \left[\sum_{k\nu} (\partial^2\epsilon)^{\nu\nu}_k \Theta(-E^\nu_k) + \sum_{k\nu'\neq\nu} \left|(\partial\epsilon)^{\nu\nu'}_k\right|^2 \frac{\Theta(E^{\nu'}_k) - \Theta(E^\nu_k)}{\omega + i\Gamma_{el} + E^\nu_k - E^{\nu'}_k} \right] \right\}. \tag{17}$$

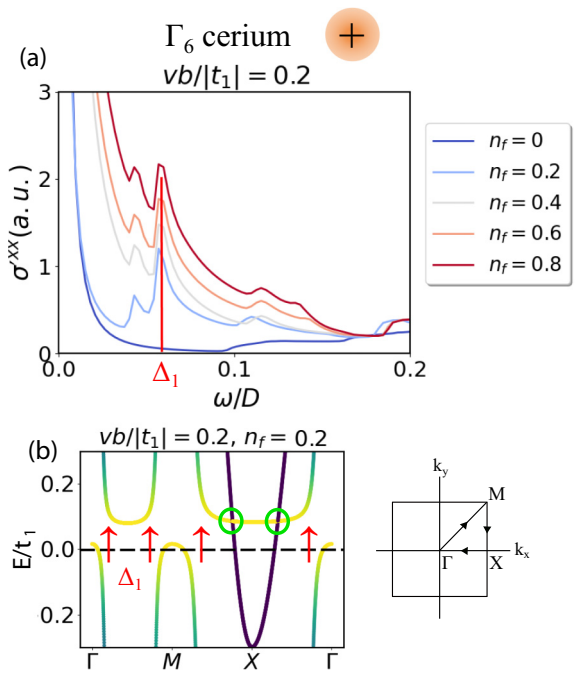

FIG. 11. (a) Optical conductivity for Γ_6 cerium with $vb/|t_1| = 0.2$. (b) Band structure for Γ_6 cerium with $vb/|t_1| = 0.2$ and $n_f = 0.2$, which shows the gap Δ_1 and the band crossing with green circle.

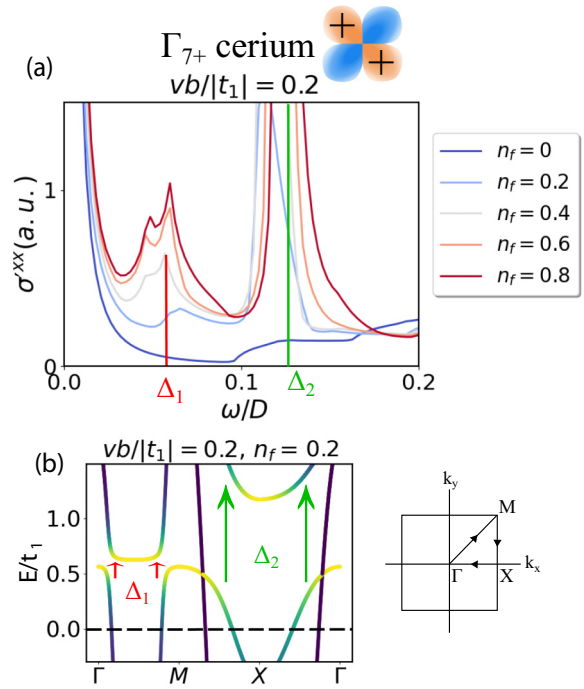

FIG. 12. (a) Optical conductivity for Γ_{7+} cerium with $vb/|t_1| = 0.2$. (b) Band structure for Γ_{7+} cerium with $vb/|t_1| = 0.2$ and $n_f = 0.2$, which shows the two gaps Δ_1 and Δ_2.

With $\Theta(x)$, the Heaviside function and

$$(\partial^2\epsilon)_k^{\nu\nu'} = \sum_{aa'} \frac{\partial^2\epsilon_k^{aa'}}{\partial k_x^2} a_k^{\nu a} \left(a_k^{a'\nu'}\right)^*,$$
$$(\partial\epsilon)_k^{\nu\nu'} = \sum_{aa'} \frac{\partial\epsilon_k^{aa'}}{\partial k_x} a_k^{\nu a} \left(a_k^{a'\nu'}\right)^*, \tag{18}$$

where $a_k^{a'\nu}$ stands for the coefficients between the orbital basis $a' = x, y, f$ and the band basis $\nu = 1, 2, 3$ which diagonalizes the matrix M_k. Equation (17) is equivalent to the expressions of [55,56] with the use of the Cauchy principal value P: $1/(\omega + i\Gamma_{el}) = P(1/\omega) + i\pi\delta(\omega)$ in the limit $\Gamma_{el} \ll 1$. Γ_{el} is associated with the time of flight between two collisions in the formulation of the kinetic equation, and thus with the temperature. In [56], the authors set $\Gamma_{el} = 20$ meV to study the optical conductivity of iron-based superconductors. Since heavy-fermion physics is generally at low temperature, and since the theoretical Kondo temperature for the effective model parameters we study here $vb/|t_1| = 0.2$ is $T_0 = 4(vb)^2/W \approx 10$ K ≈ 1 meV, we fix $\Gamma_{el} = 1$ meV.

For the case of Γ_6 cerium [see Fig. 11(a)], we observe two different features. First, the apparition of a double peak in $c_{k\sigma}^{\nu} = d_{k\sigma}^{\nu z}$ dependent of the cerium concentration, that corresponds to the hybridization gap between the f band and the lower d band Δ_1 [see Fig. 11(b)]. This double peak is characteristic of heavy-fermion compounds and is called "mid-infrared peaks" in the literature [57]. Second, a big contribution appears at very low frequency between $n_f = 0.2$ and 0.4, associated to the complete filling of the hole pockets. One can show that this contribution does not correspond to the Drude peak because it does not vary upon decreasing the scattering rate Γ_{el} (not shown). A similar situation is reported in [19], where the crossing between the f band and the conduction band above the Fermi level leads to a peak in optical conductivity. For the model studied here, the crossing between the f level and the lower d band comes closer to the Fermi energy as n_f increases, and in particular shows this big contribution for $n_f > 0.25$, which corresponds to the condition $\lambda - \mu < 0$ [see Fig. 7(b)].

For the case of Γ_{7+} [see in Fig. 12(a)], we remark several peaks at low frequency, corresponding to different hybridization gaps [see Fig. 12(b)]. The first double peak at Δ_1 is similar to the case of Γ_6 cerium and corresponds to the hybridization between the f band and the lower d band. The second one, Δ_2, corresponds to the hybridization between the f band and the upper d band.

Thus, the model presents a clear distinction between the Γ_6 cerium symmetry with a double peak at Δ_1, and the Γ_{7+} cerium with the same double peak at Δ_1 and a supplementary peak at Δ_2. We remark that considerations of nonlocal Kondo coupling leads naturally to different hybridization gaps in multiband systems, as observed experimentally in CeTIn$_5$ (T = Co, Rh, Ir) compounds [20,58].

3. Raman spectroscopy

The Raman spectrum has the property of being experimentally decomposable on the basis of irreducible representations of the point symmetry group of the crystal. Moreover, these irreducible representations are associated with intensity extinctions in certain regions of reciprocal space, enabling Raman measurements to probe specific parts of the Brillouin zone, unlike optical conductivity. Raman spectroscopy

is widely used to characterize iron-based superconducting compounds [56], and permits the electronic fluctuations of these systems to be probed directly [59].

The Raman response associated to different light polarizations and measurement settings is expressed in the simplest case of effective mass approximation with the so-called Raman vertices, that has been derived of FeSCs for example in [56]. For the square lattice symmetry considered here, we have three different vertices to study:

$$\begin{aligned}\gamma_k^{A_{1g}} &= \frac{\partial^2 M_k}{\partial k_x^2} + \frac{\partial^2 M_k}{\partial k_y^2},\\ \gamma_k^{B_{1g}} &= \frac{\partial^2 M_k}{\partial k_x^2} - \frac{\partial^2 M_k}{\partial k_y^2},\\ \gamma_k^{B_{2g}} &= \frac{\partial^2 M_k}{\partial k_x \partial k_y} + \frac{\partial^2 M_k}{\partial k_y \partial k_x},\end{aligned} \tag{19}$$

where M_k refers to the Hamiltonian matrix elements in the orbital basis of Eq. (11). Whereas the Raman vertices are easily derived in the orbital basis, the physical information is clearer in the band basis where each vertex is associated to an interband transition. Denoting $(\gamma_k^X)^{\nu\nu'}$ the Raman vertex of symmetry $X \in \{A_{1g}, B_{1g}, B_{2g}\}$ between the band ν and the band ν', we have

$$\left(\gamma_k^X\right)^{\nu\nu'} = \sum_{aa'} \left(\gamma_k^X\right)^{aa'} a_k^{\nu a} \left(a_k^{a'\nu'}\right)^*, \tag{20}$$

where $a_k^{a'\nu}$ stands for the coefficient from the orbital basis $a' = x, y, f$ and the band basis $\nu = 1, 2, 3$.

In the effective mass approximation, the Raman spectrum $\chi_X''(\omega)$ at $T = 0$ is obtained from the imaginary part of the density-density correlation function [56]:

$$\begin{aligned}\chi_X''(\omega) &= \mathrm{Im}[\chi_X(q=0, i\Omega)_{i\Omega\to\omega+i\Gamma_{el}}],\\ X &= \{A_{1g}, B_{1g}, B_{2g}\},\\ \chi_X(q=0, i\Omega) &= \int_0^\beta d\tau\, e^{-i\Omega\tau} \sum_{aa'bb'k} \left\langle \left(\gamma_k^X\right)^{aa'} \left(\gamma_k^X\right)^{bb'} \right.\\ &\quad \left. \times\ c_k^{a\dagger}(\tau) c_k^{a'}(\tau) c_k^{b\dagger}(0) c_k^{b'}(0) \right\rangle\\ &= \sum_{k\nu\neq\nu'} \left|\left(\gamma_k^X\right)^{\nu\nu'}\right|^2 \frac{\Theta\left(E_k^{\nu'}\right) - \Theta\left(E_k^{\nu}\right)}{i\Omega + E_k^{\nu} - E_k^{\nu'}}.\end{aligned} \tag{21}$$

One can remark a similarity between the expression of $\chi_X''(\omega)$ at Eq. (21) and the second term of the optical conductivity $\sigma'(\omega)$ in Eq. (17). This correspondence between the spectrum of optical conductivity and the Raman spectrum $\omega\sigma'(\omega) \propto \chi''(\omega)$ is discussed in [60], and is valid for isotropic systems. We thus expect to find some similar features between the results for those two probes, and in particular the peaks associated to Kondo hybridization gaps.

As for the optical conductivity, we fix $\Gamma_{el} = 1$ meV. On top of the Raman spectra, we analyze the interband Raman vertices $(\gamma_k^X)^{\mu\mu'}$. From the symmetry considerations available in Appendix A, one can determine the symmetry of the bands on the high-symmetry path $\Gamma \to M \to X \to \Gamma$, and thus fix the interband transition rules. Combined to the analysis of Raman vertices, this permits us to discuss in detail the Raman spectra. We will consider Raman shifts at low energy $\omega \leqslant 2000\ \mathrm{cm}^{-1} \approx 3|t_1|$ for our model parameters. First and foremost, we consider the undoped model without cerium.

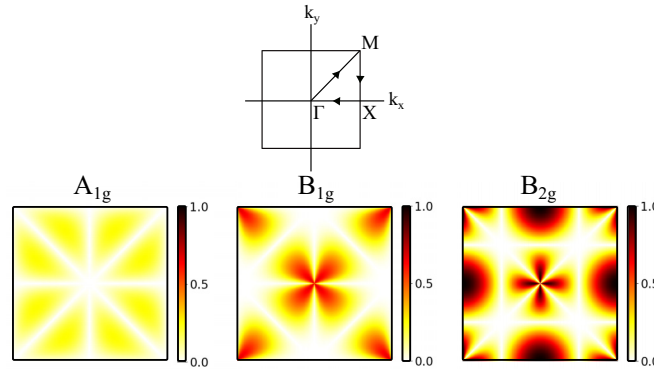

FIG. 13. Raman vertices in the Brillouin zone for each symmetry, normalized by the maximum of the three vertices, for the model without cerium.

We observe that the A_{1g} Raman vertex is the weakest (see Fig. 13), that the B_{1g} vertex contributes mostly in the $\Gamma \to M$ region, in contrary to the B_{2g} vertex that contributes mostly in the $M \to X \to \Gamma$ path. This can be understood directly from symmetry considerations on the interband transitions in the high-symmetry contour, as discussed in Appendix A. Thus, we expect the A_{1g} response to be the weakest (see Fig. 14).

For the Γ_6 cerium, we will first consider the double peak associated to $\Delta_1 \approx 500\ \mathrm{cm}^{-1}$. As this double peak involves interband transitions between the lower d band and the f band, we plot the associated interband Raman vertices $(\gamma_k^X)^{01}$ (see Fig. 15). Furthermore, we can restrict ourselves to parts of the Brillouin zone corresponding to excitations of energy

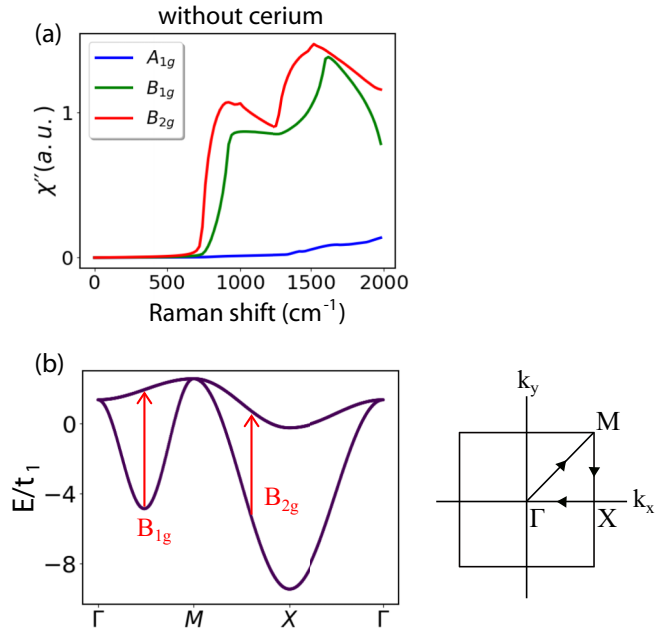

FIG. 14. (a) Raman spectrum χ'' for the three symmetries $\{A_{1g}, B_{1g}, B_{2g}\}$. (b) Band structure on the high-symmetry contour where the symmetry of interband transitions are indicated.

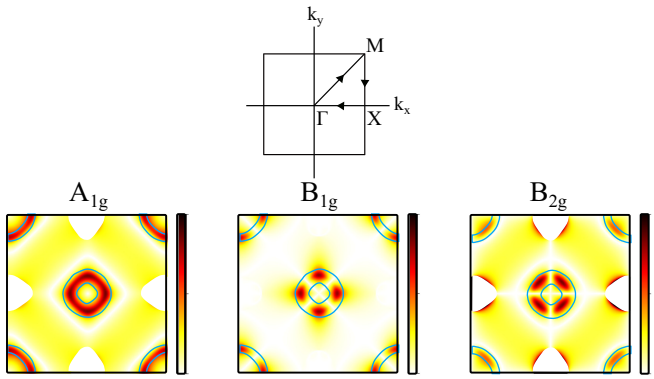

FIG. 15. Interband Raman vertices $(\gamma_k^X)^{01}$ in the Brillouin zone for each symmetry, normalized by the maximum of the three vertices, for a Γ_6 cerium and $vb/|t_1| = 0.2$, $n_f = 0.8$. For the regions in which there is band crossing and thus change in the order of the band, the vertex intensity is set to zero. The selected part of the Brillouin zone corresponds to energies $\Delta_1 - 200\ \text{cm}^{-1} \leqslant \Delta E = E_1 - E_0 \leqslant \Delta_1 + 200\ \text{cm}^{-1}$.

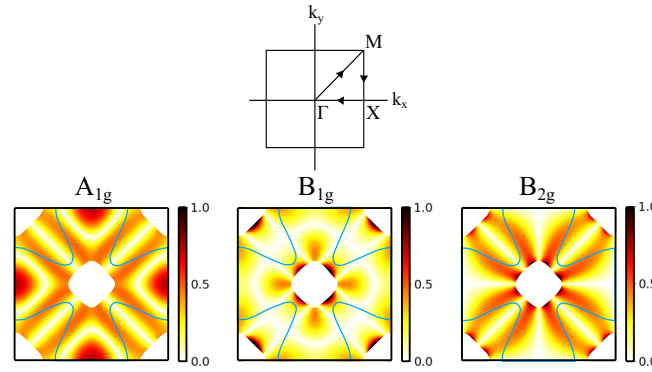

FIG. 17. Raman vertices $(\gamma_k^X)^{21}$ in the Brillouin zone for each symmetry, normalized by the maximum of the three vertices, for a Γ_{7+} cerium and $vb/|t_1| = 0.2$ $n_f = 0.8$. For the regions in which there is band crossing and thus change in the order of the band, the vertex intensity is set to zero. The selected part of the Brillouin zone corresponds to energies $\Delta_2 - 200\ \text{cm}^{-1} \leqslant \Delta E = E_2 - E_1 \leqslant \Delta_2 + 200\ \text{cm}^{-1}$.

$\Delta_1 \pm 200\ \text{cm}^{-1}$. In Fig. 15 we remark a similar contribution for the three Raman vertices in this region. Thus, we expect a similar contribution in the Raman spectra for A_{1g}, B_{1g}, and B_{2g} channels.

The Raman spectra for $0 \leqslant \omega \leqslant 2000\ \text{cm}^{-1}$ are shown in Fig. 16. For the double peak around $\Delta_1 \approx 500\ \text{cm}^{-1}$, we observe the strongest response in the B_{2g} channel, but the intensity is quite comparable with the other ones, in accordance with the Raman vertices. Furthermore, we observe a peak at very low Raman shift $\omega \approx 30\ \text{cm}^{-1}$, mostly of the B_{2g} type. As discussed from the optical conductivity, this peak corresponds to the crossing points between the f band and the upper d band in $M \to X \to \Gamma$, associated to a B_{2g} transition [see Fig. 16(b)].

For Γ_{7+} cerium (see Figs. 17 and 18), we will mostly look at the second peak associated to Δ_2 and observed in optical conductivity. As this peak involves interband transitions between the upper d band and the f band, we plot the associated interband Raman vertices $(\gamma_k^X)^{21}$ (see Fig. 17). Furthermore,

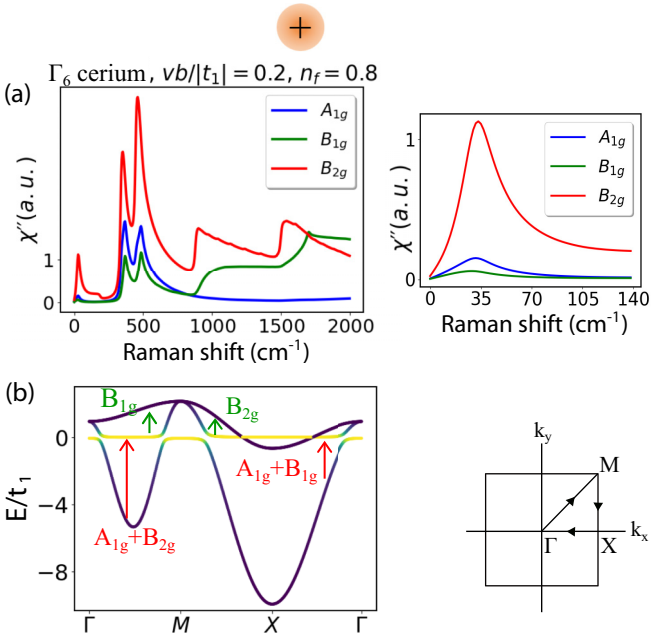

FIG. 16. (a) Raman spectra χ'' for the three symmetries $\{A_{1g}, B_{1g}, B_{2g}\}$, in the case of a Γ_6 cerium with $vb/|t_1| = 0.2$, $n_f = 0.8$. (b) Band structure for a Γ_6 cerium with $vb/|t_1| = 0.2$, $n_f = 0.8$, and symmetry of the interband transitions.

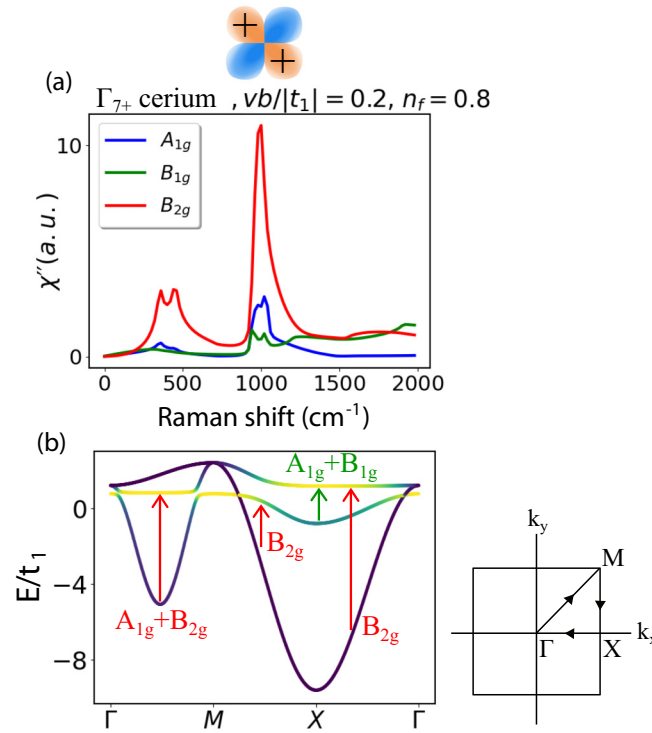

FIG. 18. (a) Raman spectra χ'' for the three symmetries $\{A_{1g}, B_{1g}, B_{2g}\}$, in the case of a Γ_{7+} cerium with $vb/|t_1| = 0.2$, $n_f = 0.8$. (b) Band structure for a Γ_{7+} cerium with $vb/|t_1| = 0.2$, $n_f = 0.8$, and symmetry of the interband transitions.

we can restrict ourselves to parts of the Brillouin zone corresponding to excitations of energy $\Delta_2 \pm 200\ \mathrm{cm}^{-1}$ as shown in Fig. 17. This time we remark a strong contribution of the A_{1g} and B_{2g} vertices compared to the B_{1g} one, even if the B_{2g} vertex intensity is zero on the $M \to X \to \Gamma$ line, which is imposed by symmetry.

The Raman spectra for $0 \leqslant \omega \leqslant 2000\ \mathrm{cm}^{-1}$ are shown in Fig. 18. We remark that the B_{2g} contribution dominates strongly. The smallest contribution comes from the B_{1g} channel in accordance with the Raman vertices.

In their study of the Raman spectra of the $5f$-electron heavy-fermion compound URu_2Si_2, the authors of [21] associate the maxima of the E_g interband Raman vertex to the d-wave symmetry of the Kondo pseudogap. The study presented here shows that the association of the vertex symmetry and the Kondo pseudogap symmetry can be complex in multiband systems. Nevertheless, we showed that the Raman spectra strongly differ upon the symmetry chosen for the cerium orbital. In particular, for the Γ_{7+} cerium symmetry the B_{2g} contribution dominates (see Fig. 18), whereas for the Γ_6 cerium symmetry all A_{1g}, B_{1g}, and B_{2g} have comparable intensities (see Fig. 16).

Furthermore, the low-frequency peak for the cerium case Γ_6 gives an additional indication of the Lifshitz transition associated to the complete filling of the hole pockets. The study of the Raman spectrum is already known to be able to signal the presence of a Lifshitz transition, for example, on $BaFe_{2-x}Co_xAs_2$ [61].

IV. CONCLUSION

In this work, motivated by iron-based superconductors of ZrCuSiAs structure containing cerium atoms, we have considered Kondo coherence effects with nonlocal fd hybridization, arising in a two-dimensional square lattice model with cerium ions located at the center of iron plaquettes. This nonlocal hybridization leads to a k dependence of the Kondo gap in reciprocal space, which leads to an unconventional Fermi liquid at low temperatures as discussed in [19].

One of our principal results is stated as the pocket-selective doping from cerium f electrons. It arises from nonlocal fd hybridization in a multiband system, and its relation to the orbital and symmetry contents of a given material has been clarified (see Appendix A). The band crossings and Fermi-surface reconstruction proposed here should be measurable in any measurement sensitive to Fermi surfaces: ARPES, quantum oscillations, Compton scattering [62]. In particular, we showed for a Γ_{7+} symmetry that the cerium f electrons will populate the electron pockets, whereas for a Γ_6 symmetry the cerium f electrons will populate the hole pockets. We propose the Γ_6 cerium symmetry for the ground state of CeFePO, as it reproduces the hybridization with the hole pockets observed in [7]. Furthermore, we expect that these results could apply to the high-pressure paramagnetic phase of CeFeAsO above 5 GPa, for which a doping from cerium f electrons has been proposed in [12].

Second, we have identified a Lifshitz transition corresponding to the complete filling of the hole pockets in the case of Γ_6 cerium symmetry. This transition can be induced either by doping or by an increase of the fd hybridization. The Lifshitz transition induced by increase of the fd hybridization could be achieved through the application of pressure on the compound. We expect that this transition could be observed in magnetoresistance [63] and thermopower measurements [64] at low temperature.

Third, we proposed several other experimental probes that could be sensitive to the cerium orbital symmetry in the nonlocal fd hybridization scenario. On one hand, we studied thermodynamic probes such as the density of states at the Fermi level and the static spin susceptibility. We showed that the density of states greatly differs between doping with a Γ_{7+} and Γ_6 cerium symmetry, what we attributed to the Lifshitz transition predicted for the Γ_6 cerium. The static spin susceptibility permits also to distinguish the two cases, with a peak at the $M = (\pi, \pi)$ point of the Brillouin zone for the Γ_6 cerium which is absent for the Γ_{7+} indicating different nesting conditions and thus being related to the difference of Fermi-surface reconstruction. On the other hand, we studied spectroscopic probes such as the optical conductivity and the Raman spectra. The optical conductivity results lead to a clear distinction between the two cases, namely, the presence of a mid-IR double peak at Δ_1 for the Γ_6 cerium symmetry, whereas the case of Γ_{7+} cerium shows the same double peak at Δ_1 with an additional third peak at higher energy Δ_2. Finally, the Raman spectra showed some complementary results to the optical conductivity with the presence of the same peaks and a supplementary information associated to the symmetry of the interband transitions. For the Γ_6 cerium symmetry, the interband transitions involve the three A_{1g}, B_{1g}, and B_{2g} channels, whereas in the case of Γ_{7+} cerium symmetry they are mostly of the B_{2g} character.

The results can be extended to other families of compounds with similar structures, with the addition of three-dimensional effects for compounds of $ThCr_2Si_2$ structure, as studied in [65] for the iron-based superconductor $BaFe_2As_2$. For compounds of $ThCr_2Si_2$ structure in collapsed phase like $CeCu_2Si_2$ [66] or $CeRu_2Si_2$ [67], one has to consider completely different Fermi surfaces in the absence of f electrons because of the silicon-silicon bond along the c axis. The same nonlocal Kondo coupling from a cerium in the center of indium plaquettes is adapted to discuss $CeTIn_5$ compounds (T = Co, Rh, Ir) [68], where the symmetry of the cerium orbital has been recently proposed to be associated with the appearance of the superconducting regime [69]. The focus on cerium atom as the f-electron carrier can easily be generalized. The square plane group has four representations of dimension 1: $\{A_{1g}, A_{2g}, B_{1g}, B_{2g}\}$. Only the A_{2g} representation has not been studied here, and could be useful to discuss compounds containing ytterbium atoms, where the $J = \frac{7}{2}$ multiplet splits into four Kramers doublets under a tetragonal crystal field. With this last case, the model would apply equally well for cerium, ytterbium, uranium, or neptunium atoms as long as the physics is dominated by a Kramers doublet well separated from the others in energy.

In a slightly broader context, nonlocal Kondo coupling considerations also deserve to be applied to compounds of skutterudite structure, such as $CeOs_4Sb_{12}$ [70] or $PrOs_4Sb_{12}$ [71], where the rare-earth atom is located in the center of an antimony cage. In $CeOs_4Sb_{12}$, the hybridization gap between the f level of cerium and the conduction bands is observed to

vary in the Brillouin zone from 24 meV with the α pocket to 56 meV with the β pocket [72], in agreement with the nonlocal Kondo coupling scenario. We therefore expect that the difference in symmetry between the f levels of praseodymium and cerium could be taken into account to explain the difference in behavior between the Kondo insulator $CeOs_4Sb_{12}$ and the heavy-fermion superconductor $PrOs_4Sb_{12}$, in addition to the differences between the $4f^1$ and $4f^2$ configuration already discussed in [72], for example.

Finally, a symmetry change for the low-energy doublet of cerium has been evoked to explain the ferromagnetic to antiferromagnetic transition observed in CeRuPO under pressure [73]. Our approach proposes a clear mechanism to understand how a change in cerium orbital symmetry can lead to significant effects on the hybridization between cerium and conduction electrons.

APPENDIX A: SYMMETRY ASPECTS OF THE MODEL

We analyze the k dependence of the cerium-iron hybridization in the high-symmetry contour of the Brillouin zone $\Gamma \to R \to X \to \Gamma$ defined in Fig. 2. To do so we use standards of $k \cdot p$ theory [74,75], which relies on associating a symmetry quantum number to each band in order to invoke the Wigner-Eckart theorem. To translate symmetry operations g of the symmetry group G in real space to symmetry operations in k space, we use the preservation of the identity that defines the reciprocal lattice vector under symmetry operations, for $\vec{r}$ a Bravais vector and $\vec{k}$ a reciprocal lattice vector [74]:

$$\vec{k}\cdot\vec{r} = 2\pi \Rightarrow \vec{k}\cdot(g\vec{r}) = (g^{-1}g\vec{k})\cdot(g\vec{r}) = (g^{-1}\vec{k})\cdot\vec{r} \quad \forall\, g \in G. \tag{A1}$$

Thus, the set of all symmetry operations is the same in real space and in k space. Let us take two examples. At the Γ point, all symmetry operations of the square space group D_4 leave the k vector (0,0) invariant. But the d^{xz} orbital is not a representation of D_4 since it is transformed in d^{yz} under the action of the diagonal mirror σ^+. However, the doublet $\{d^{xz}, d^{yz}\}$ is a representation of D_4, of dimension 2. We thus deduce that the two Fe d bands are degenerate in Γ.

Between Γ and M (let us call this region Λ), the only operations that leave a vector $k \in \Lambda \Leftrightarrow k_x = k_y$ invariant are the identity E and the diagonal mirror σ^+, forming a group $\mathbb{Z}_2$. In order to know how the two degenerate bands in Γ, that are an irreducible representation of D_4, evolve into irreducible representations of the symmetry group in Λ, we have to look on the character tables. We obtain the compatibility relations by imposing that the characters should be equal to each other (see Table I).

Thus, the representation of dimension 2 at the Γ point becomes two representations of dimension 1 of $\mathbb{Z}_2$: $C \to e \oplus e'$, having different eigenvalues under the symmetry operation σ_+. Since we know that $\sigma_+|d^{xz}\rangle = |d^{yz}\rangle$, we can build linear combinations having different eigenvalues like $e = |d^{xz}\rangle + |d^{yz}\rangle \to \sigma_+ e = +e$ and $e' = |d^{xz}\rangle - |d^{yz}\rangle \to \sigma_+ e' = -e'$, which are the bonding and antibonding combinations. Finally, since the Γ_6 and Γ_{7+} cerium orbitals are both symmetric under σ_+, so the f band will hybridize with the bonding combination and not with the antibonding one. The situation is reversed for the Γ_{7-} case. The same reasoning applies to the paths $M \to X$ and $X \to \Gamma$ that also admit a symmetry $\mathbb{Z}_2 = \{E, \sigma_x\}$ and $\mathbb{Z}_2 = \{E, \sigma_y\}$, as shown in Fig. 19.

TABLE I. Compatibility relations between D_4 and $\mathbb{Z}_2$. Irreps is the short notation for irreducible representations.

irreps of D_4 (Γ)	E	σ_+	irreps of $\mathbb{Z}_2$ (Λ)
e	1	1	
e'	1	−1	
A_1	1	1	e
A_2	1	−1	e'
B_1	1	−1	e'
B_2	1	1	e
C	2	0	$e \oplus e'$

Interband transition symmetry and Raman spectra

In order to obtain the allowed interband transitions, one has to look at the character table of the square plane group D_4 (see Table II).

For example, for the two-band model (without cerium), we have two different regions to study. In the $\Gamma \to M$ region, since the two bands have a different symmetry according to the σ^+ symmetry operation, then the associated Raman transition has to be of character -1 for the $\sigma_{+,-}$ equivalence class, so B_{1g}. In the $M \to X \to \Gamma$ region, the two bands have a different symmetry according to $\sigma_{x,y}$ and the associated Raman transition will thus also be of character -1 for this equivalence class, which is B_{2g}. The same reasoning is easily applicable for the models with cerium, where one has to take into account Raman transitions of $+1$ character when the two bands have the same symmetry, i.e., when hybridization between the flat level and the conduction band is allowed. The four one-dimensional representations of D_4 are shown in Fig. 20.

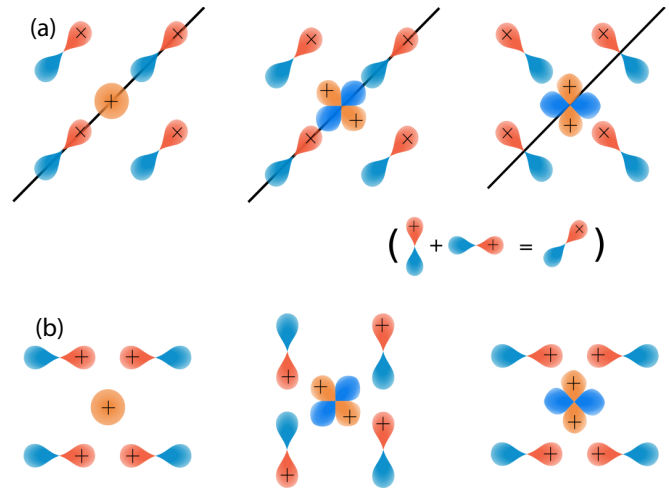

FIG. 19. Allowed hybridization with the bonding and antibonding combination in the $\Gamma \to R$ line close to the Γ point (a), and allowed hybridization around the X point (b).

TABLE II. Character table of D_4.

D_4	n_c	c	A_1	A_2	B_1	B_2	C
	1	E	1	1	1	1	2
	1	C_2	1	1	1	1	−2
	2	$C_4^{1,3}$	1	1	−1	−1	0
	2	$\sigma_{x,y}$	1	−1	1	−1	0
	2	$\sigma_{+,-}$	1	−1	−1	1	0

APPENDIX B: OPTICAL CONDUCTIVITY CALCULATION

We consider a gauge in which the scalar potential is zero $\phi = 0$, so that electric $\vec{E} = i\omega\vec{A}$ and magnetic $\vec{B} = \vec{\nabla} \times \vec{A}$ fields are determined from the vector potential $\vec{A}$. In order to express the interaction between the quasiparticles of the effective Hamiltonian (9) and light, we take the compact notation, with $c^x_{i\sigma} = d^{xz}_{i\sigma}$, $c^y_{i\sigma} = d^{yz}_{i\sigma}$, and $c^f_{i\sigma} = f_{i\sigma}$. The Hamiltonian (9) is written as

$$\mathcal{H}_{\text{eff}} = \sum_{ija a'\sigma} t_{ij}^{aa'} c_{i\sigma}^{a\dagger} c_{j\sigma}^{a'} + \epsilon_0 = \sum_{kaa'\sigma} \epsilon_k^{aa'} c_{k\sigma}^{a\dagger} c_{k\sigma}^{a'} + \epsilon_0$$
$$= \sum_{k\mu\sigma} E_k^{\mu} c_{k\sigma}^{\mu\dagger} c_{k\sigma}^{\mu} + \epsilon_0, \tag{B1}$$
$$\mathcal{H} = \sum_{ij\alpha\alpha'\sigma} \left(t_{ij}^{\alpha\alpha'} - \mu\delta_{ij}\delta^{\alpha\alpha'}\right) d_{i\sigma}^{\alpha\dagger} d_{j\sigma}^{\alpha'}. \tag{B2}$$

It has been shown recently that dipolar effects might be important when dealing with external electromagnetic field on tight-binding models with a limited number of bands [76]. In our case, we used the simpler formulation in which the effect of external electric field is weak and homogeneous in space associated to a vector potential directed along the x axis, $\vec{A} = A^x \vec{e}_x$ is done with Peierls substitution for the transfer integrals [56] (with $e = c = \hbar = 1$):

$$t_{ij}^{aa'} \to t_{ij}^{aa'} \exp\left(-i\int_{\vec{r}_i}^{\vec{r}_j} \vec{A}\cdot d\vec{r}\right) \approx t_{ij}^{aa'} \exp(-i\vec{A}\cdot(\vec{r}_i - \vec{r}_j))$$
$$\approx t_{ij}^{aa'}\left(1 - i\vec{A}\cdot(\vec{r}_i - \vec{r}_j) - \frac{1}{2}(\vec{A}\cdot(\vec{r}_i - \vec{r}_j))^2 + \cdots\right). \tag{B3}$$

Thus, the current operator is obtained by identifying the correction to the kinetic energy induced by the field

$$j^x_{q=0} = -\frac{\partial \mathcal{H}_{\text{eff}}(A^x)}{\partial A^x}$$
$$= -i\sum_{k\sigma aa'} \frac{\partial \epsilon_k^{aa'}}{\partial k_x} c_{k\sigma}^{a\dagger} c_{k\sigma}^{a'} - A^x \sum_{k\sigma aa'} \frac{\partial^2 \epsilon_k^{aa'}}{\partial k_x^2} c_{k\sigma}^{a\dagger} c_{k\sigma}^{a'} + \cdots. \tag{B4}$$

And the conductivity defined by the linear response coefficient for the induced current $\langle j^x_{q=0}\rangle = \sigma^{xx}(\omega) E^x_{q=0}(\omega)$, with the electric field $E^x(\omega) = A^x(\omega) \times (i\omega - \Gamma_{el})$. Up to first order in A^x, the mean value of the current operator is taken from Kubo formula, and the optical conductivity is written as [77]

$$\sigma^{xx}(\omega) = \frac{i}{\omega + i\Gamma_{el}}[D + \Pi(i\Omega)]_{i\Omega\to\omega+i\Gamma_{el}},$$
$$D = \sum_{k\sigma aa'} \frac{\partial^2 \epsilon_k^{aa'}}{\partial k_x^2} \langle c_{k\sigma}^{a\dagger} c_{k\sigma}^{a'}\rangle = \frac{1}{\beta}\sum_{kaa'\sigma i\omega} \frac{\partial^2 \epsilon_k^{aa'}}{\partial k_x^2} G^{aa'}(k, i\omega),$$
$$\Pi(i\Omega) = -\int_0^\beta d\tau\, e^{-i\Omega\tau} \langle \mathcal{T}_\tau j^x_{q=0}(\tau) j^x_{q=0}(0)\rangle$$
$$= \frac{1}{\beta}\sum_{kaa'\sigma i\omega} \frac{\partial \epsilon_k^{aa'}}{\partial k_x} \frac{\partial \epsilon_k^{a'a}}{\partial k_x} G^{aa'}(k, i\omega) G^{a'a}(k, i\omega + i\Omega), \tag{B5}$$

where $\mathcal{T}_\tau$ is the time ordering. We are interested in the real part of the conductivity $\sigma(\omega) = \sigma'(\omega) + i\sigma''(\omega)$. At $T = 0$, we have

$$\sigma'^{xx}(\omega) = \text{Re}\left\{\frac{2i}{\omega + i\Gamma_{el}}\left[\sum_{k\mu}(\partial^2\epsilon)_k^{\mu\mu}\Theta(-E_k^\mu) + \sum_{k\mu'\neq\mu} |(\partial\epsilon)_k^{\mu\mu'}|^2 \frac{\Theta(E_k^{\mu'}) - \Theta(E_k^\mu)}{\omega + i\Gamma + E_k^\mu - E_k^{\mu'}}\right]\right\}. \tag{B6}$$

With $\Theta(x)$ the Heaviside function and

$$(\partial^2\epsilon)_k^{\mu\mu'} = \sum_{aa'} \frac{\partial^2 \epsilon_k^{aa'}}{\partial k_x^2} a_k^{\mu a} \left(a_k^{a'\mu'}\right)^*,$$
$$(\partial\epsilon)_k^{\mu\mu'} = \sum_{aa'} \frac{\partial \epsilon_k^{aa'}}{\partial k_x} a_k^{\mu a} \left(a_k^{a'\mu'}\right)^*, \tag{B7}$$

where $a_k^{a'\mu}$ are the coefficient between the orbital basis $a' = x, y, f$ and the band basis $\mu = 1, 2, 3$ which diagonalizes M_k. Equation (B6) is equivalent to the expressions of [55,56] with $1/(\omega + i\Gamma_{el}) = P(1/\omega) + i\pi\delta(\omega)$, in the limit $\Gamma_{el} \ll 1$.

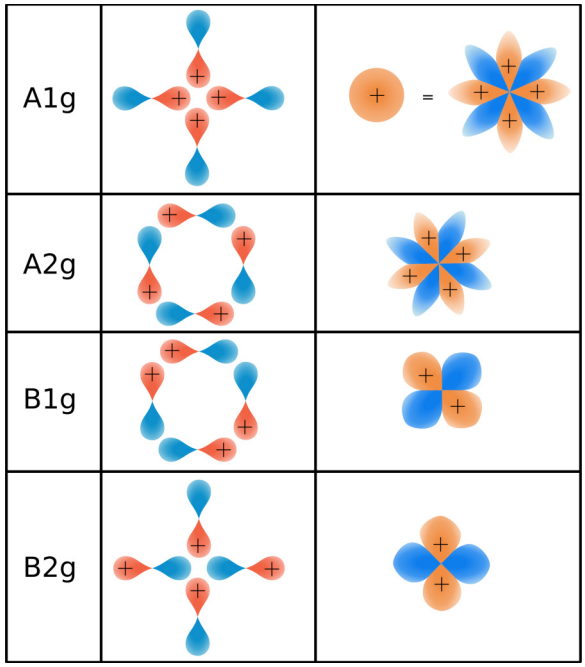

FIG. 20. The four one-dimensional representations of the square plane group, showed with iron d orbitals and rare-earth f orbital.

[1] F. Steglich, J. Aarts, C. D. Bredl, W. Lieke, D. Meschede, W. Franz, and H. Schäfer, Superconductivity in the presence of strong Pauli paramagnetism: $CeCu_2Si_2$, Phys. Rev. Lett. **43**, 1892 (1979).

[2] T. Park, F. Ronning, H. Yuan, M. Salamon, R. Movshovich, J. Sarrao, and J. Thompson, Hidden magnetism and quantum criticality in the heavy fermion superconductor $CeRhIn_5$, Nature (London) **440**, 65 (2006).

[3] G. Stewart, Non-Fermi-liquid behavior in *d*-and *f*-electron metals, Rev. Mod. Phys. **73**, 797 (2001).

[4] D. Hafner, P. Khanenko, E.-O. Eljaouhari, R. Küchler, J. Banda, N. Bannor, T. Lühmann, J. F. Landaeta, S. Mishra, I. Sheikin, E. Hassinger, S. Khim, C. Geibel, G. Zwicknagl, and M. Brando, Possible quadrupole density wave in the superconducting Kondo lattice $CeRh_2As_2$, Phys. Rev. X **12**, 011023 (2022).

[5] S. Stewart, Heavy-fermion systems, Rev. Mod. Phys. **56**, 755 (1984).

[6] G. Zwicknagl, Quasi-particles in heavy fermion systems, Adv. Phys. **41**, 203 (1992).

[7] M. G. Holder, A. Jesche, P. Lombardo, R. Hayn, D. V. Vyalikh, S. Danzenbächer, K. Kummer, C. Krellner, C. Geibel, Y. Kucherenko, T. K. Kim, R. Follath, S. L. Molodtsov, and C. Laubschat, CeFePO: *f-d* hybridization and quenching of superconductivity, Phys. Rev. Lett. **104**, 096402 (2010).

[8] P. A. Lee, N. Nagaosa, and X. G. Wen, Doping a Mott insulator: Physics of high-temperature superconductivity, Rev. Mod. Phys. **78**, 17 (2006).

[9] P. Hirschfeld, M. Korshunov, and I. Mazin, Gap symmetry and structure of Fe-based superconductors, Rep. Prog. Phys. **74**, 124508 (2011).

[10] L. Pourovskii, V. Vildosola, S. Biermann, and A. Georges, Local moment vs. Kondo behavior of the 4*f*-electrons in rare-earth iron oxypnictides, Europhys. Lett. **84**, 37006 (2008).

[11] E. M. Brüning, C. Krellner, M. Baenitz, A. Jesche, F. Steglich, and C. Geibel, CeFePO: A heavy fermion metal with ferromagnetic correlations, Phys. Rev. Lett. **101**, 117206 (2008).

[12] K. Mydeen, A. Jesche, K. Meier-Kirchner, U. Schwarz, C. Geibel, H. Rosner, and M. Nicklas, Electron doping of the iron-arsenide superconductor CeFeAsO controlled by hydrostatic pressure, Phys. Rev. Lett. **125**, 207001 (2020).

[13] F. Bernardini, G. Garbarino, A. Sulpice, M. Núñez-Regueiro, E. Gaudin, B. Chevalier, M. A. Méasson, A. Cano, and S. Tencé, Iron-based superconductivity extended to the novel silicide LaFeSiH, Phys. Rev. B **97**, 100504(R) (2018).

[14] D. Lu, M. Yi, S. Mo, A. Erickson, J. Analytis, J. Chu, D. Singh, Z. Hussain, T. Geballe, I. Fisher *et al.*, Electronic structure of the iron-based superconductor LaOFeP, Nature (London) **455**, 81 (2008).

[15] S. Maiti and A. Chubukov, Superconductivity from repulsive interaction, in *AIP Conference Proceedings* (American Institute of Physics, Melville, NY, 2013), Vol. 1550, pp. 3–73.

[16] S. Barnes, New method for the Anderson model, J. Phys. F: Met. Phys. **6**, 1375 (1976).

[17] P. Coleman, New approach to the mixed-valence problem, Phys. Rev. B **29**, 3035 (1984).

[18] A. Wugalter, Y. Komijani, and P. Coleman, Large-N approach to the two-channel Kondo lattice, Phys. Rev. B **101**, 075133 (2020).

[19] H. Weber and M. Vojta, Heavy-fermion metals with hybridization nodes: Unconventional Fermi liquids and competing phases, Phys. Rev. B **77**, 125118 (2008).

[20] K. S. Burch, S. V. Dordevic, F. P. Mena, A. B. Kuzmenko, D. Van Der Marel, J. L. Sarrao, J. R. Jeffries, E. D. Bauer, M. B. Maple, and D. N. Basov, Optical signatures of momentum-dependent hybridization of the local moments and conduction electrons in Kondo lattices, Phys. Rev. B **75**, 054523 (2007).

[21] J. Buhot, X. Montiel, Y. Gallais, M. Cazayous, A. Sacuto, G. Lapertot, D. Aoki, N. E. Hussey, C. Lacroix, C. Pépin, S. Burdin, and M.-A. Méasson, Anisotropic Kondo pseudogap in URu_2Si_2, Phys. Rev. B **101**, 245103 (2020).

[22] H. Miyazaki, T. Hajiri, T. Ito, S. Kunii, and S. I. Kimura, Momentum-dependent hybridization gap and dispersive in-gap state of the Kondo semiconductor SmB_6, Phys. Rev. B **86**, 075105 (2012).

[23] P. Starowicz, R. Kurleto, J. Goraus, H. Schwab, M. Szlawska, F. Forster, A. Szytuła, I. Vobornik, D. Kaczorowski, and F. Reinert, Evidence of momentum-dependent hybridization in $Ce_2Co_{0.8}Si_{3.2}$, Phys. Rev. B **89**, 115122 (2014).

[24] Y. Nakatani, H. Aratani, H. Fujiwara, T. Mori, A. Tsuruta, S. Tachibana, T. Yamaguchi, T. Kiss, A. Yamasaki, A. Yasui, H. Yamagami, J. Miyawaki, T. Ebihara, Y. Saitoh, and A. Sekiyama, Evidence for momentum-dependent heavy-fermionic electronic structures: Soft X-ray ARPES for the superconductor $CeNi_2Ge_2$ in the normal state, Phys. Rev. B **97**, 115160 (2018).

[25] Y. Wu, Y. Zhang, F. Du, B. Shen, H. Zheng, Y. Fang, M. Smidman, C. Cao, F. Steglich, H. Yuan *et al.*, Anisotropic *c-f* hybridization in the ferromagnetic quantum critical metal $CeRh_6$ Ge_4, Phys. Rev. Lett. **126**, 216406 (2021).

[26] S. Danzenbächer, Y. Kucherenko, M. Heber, D. V. Vyalikh, S. L. Molodtsov, V. D. P. Servedio, and C. Laubschat, Wave-vector dependent intensity variations of the Kondo peak in photoemission from $CePd_3$, Phys. Rev. B **72**, 033104 (2005).

[27] W. Wu and A.-M.-S. Tremblay, *d*-wave superconductivity in the frustrated two-dimensional periodic Anderson model, Phys. Rev. X **5**, 011019 (2015).

[28] M. Sera, N. Kobayashi, T. Yoshino, K. Kobayashi, T. Takabatake, G. Nakamoto, and H. Fujii, Anisotropic pseudogap in CeNiSn and CeRhSb studied by a thermal-conductivity measurement, Phys. Rev. B **55**, 6421 (1997).

[29] H. Ikeda and K. Miyake, A theory of anisotropic semiconductor of heavy fermions, J. Phys. Soc. Jpn. **65**, 1769 (1996).

[30] J. Moreno and P. Coleman, Gap-anisotropic model for the narrow-gap Kondo insulators, Phys. Rev. Lett. **84**, 342 (2000).

[31] V. Cvetkovic and O. Vafek, Space group symmetry, spin-orbit coupling, and the low-energy effective Hamiltonian for iron-based superconductors, Phys. Rev. B **88**, 134510 (2013).

[32] S. Raghu, X. L. Qi, C. X. Liu, D. J. Scalapino, and S. C. Zhang, Minimal two-band model of the superconducting iron oxypnictides, Phys. Rev. B **77**, 220503(R) (2008).

[33] A. Amorese, A. Marino, M. Sundermann, K. Chen, Z. Hu, T. Willers, F. Choueikani, P. Ohresser, J. Herrero-Martin, S. Agrestini *et al.*, Possible multiorbital ground state in $CeCu_2Si_2$, Phys. Rev. B **102**, 245146 (2020).

[34] P. Coleman, Mixed valence as an almost broken symmetry, Phys. Rev. B **35**, 5072 (1987).

[35] S. Burdin and V. Zlatić, Multiple temperature scales of the periodic Anderson model: Slave boson approach, Phys. Rev. B **79**, 115139 (2009).

[36] P. Riseborough and J. Lawrence, Mixed valent metals, Rep. Prog. Phys. **79**, 084501 (2016).

[37] S. Burdin, A. Georges, and D. R. Grempel, Coherence scale of the Kondo lattice, Phys. Rev. Lett. **85**, 1048 (2000).

[38] Z. R. Ye, Y. Zhang, F. Chen, M. Xu, J. Jiang, X. H. Niu, C. H. P. Wen, L. Y. Xing, X. C. Wang, C. Q. Jin, B. P. Xie, and D. L. Feng, Extraordinary doping effects on quasiparticle scattering and bandwidth in iron-based superconductors, Phys. Rev. X **4**, 031041 (2014).

[39] S. Burdin and C. Lacroix, Lifshitz transition in Kondo alloys, Phys. Rev. Lett. **110**, 226403 (2013).

[40] B. Poudel, C. Lacroix, G. Zwicknagl, and S. Burdin, Photoemission signatures of coherence breakdown in Kondo alloys: dynamical mean-field theory approach, New J. Phys. **23**, 063073 (2021).

[41] I. M. Lifshitz, Anomalies of electron characteristics of a metal in the high pressure region, J. Expt. Theoor. Phys. (USSR) **38**, 1569 (1960) [Sov. Phys. JETP **11**, 1130 (1960)].

[42] M. Takahashi, D. Ootsuki, M. Horio, M. Arita, H. Namatame, M. Taniguchi, N. Saini, H. Sugawara, and T. Mizokawa, Multiband electronic structure of ferromagnetic CeRuPO, J. Phys. Soc. Jpn. **87**, 043703 (2018).

[43] C. Krellner and C. Geibel, Single crystal growth and anisotropy of CeRuPO, J. Cryst. Growth **310**, 1875 (2008).

[44] A. Jesche, C. Krellner, M. de Souza, M. Lang, and C. Geibel, Rare earth magnetism in CeFeAsO: A single crystal study, New J. Phys. **11**, 103050 (2009).

[45] J. Dai, J. X. Zhu, and Q. Si, *f*-spin physics of rare-earth iron pnictides: Influence of *d*-electron antiferromagnetic order on the heavy-fermion phase diagram, Phys. Rev. B **80**, 020505(R) (2009).

[46] Y. Yamaji, T. Misawa, and M. Imada, Quantum and topological criticalities of Lifshitz transition in two-dimensional correlated electron systems, J. Phys. Soc. Jpn. **75**, 094719 (2006).

[47] G. Mazza, M. Rösner, L. Windgätter, S. Latini, H. Hübener, A. J. Millis, A. Rubio, and A. Georges, Nature of symmetry breaking at the excitonic insulator transition: Ta_2NiSe_5, Phys. Rev. Lett. **124**, 197601 (2020).

[48] D. Pines and P. Nozières, *The Theory of Quantum Liquids* (Benjamin, New York, 1966).

[49] A. o. Abrikosov, *Introduction to the Theory of Normal Metals* (Academic, New York, 1972).

[50] T. M. McQueen, M. Regulacio, A. J. Williams, Q. Huang, J. W. Lynn, Y. S. Hor, D. V. West, M. A. Green, and R. J. Cava, Intrinsic properties of stoichiometric LaFePo, Phys. Rev. B **78**, 024521 (2008).

[51] I. I. Mazin, D. J. Singh, M. D. Johannes, and M. H. Du, Unconventional superconductivity with a sign reversal in the order parameter of $LaFeAsO_{1-x}F_x$, Phys. Rev. Lett. **101**, 057003 (2008).

[52] A. V. Chubukov, D. V. Efremov, and I. Eremin, Magnetism, superconductivity, and pairing symmetry in iron-based superconductors, Phys. Rev. B **78**, 134512 (2008).

[53] S. Graser, T. Maier, P. Hirschfeld, and D. Scalapino, Near-degeneracy of several pairing channels in multiorbital models for the Fe pnictides, New J. Phys. **11**, 025016 (2009).

[54] L. Degiorgi, The electrodynamic response of heavy-electron compounds, Rev. Mod. Phys. **71**, 687 (1999).

[55] E. Dagotto, Correlated electrons in high-temperature superconductors, Rev. Mod. Phys. **66**, 763 (1994).

[56] B. Valenzuela, M. J. Calderón, G. León, and E. Bascones, Optical conductivity and Raman scattering of iron superconductors, Phys. Rev. B **87**, 075136 (2013).

[57] D. N. Basov, R. D. Averitt, D. van Der Marel, M. Dressel, and K. Haule, Electrodynamics of correlated electron materials, Rev. Mod. Phys. **83**, 471 (2011).

[58] J. Shim, K. Haule, and G. Kotliar, Modeling the localized-to-itinerant electronic transition in the heavy fermion system $CeIrIn_5$, Science **318**, 1615 (2007).

[59] Y. Gallais and I. Paul, Charge nematicity and electronic Raman scattering in iron-based superconductors, C. R. Phys. **17**, 113 (2016).

[60] T. P. Devereaux and R. Hackl, Inelastic light scattering from correlated electrons, Rev. Mod. Phys. **79**, 175 (2007).

[61] P. Marsik, C. N. Wang, M. Rössle, M. Yazdi-Rizi, R. Schuster, K. W. Kim, A. Dubroka, D. Munzar, T. Wolf, X. H. Chen, and C. Bernhard, Low-energy interband transitions in the infrared response of $Ba(Fe_{1-x}Co_x)_2As_2$, Phys. Rev. B **88**, 180508(R) (2013).

[62] M. Güttler, K. Kummer, K. Kliemt, C. Krellner, S. Seiro, C. Geibel, C. Laubschat, Y. Kubo, Y. Sakurai, D. V. Vyalikh, and A. Koizumi, Visualizing the Kondo lattice crossover in $YbRh_2Si_2$ with Compton scattering, Phys. Rev. B **103**, 115126 (2021).

[63] H. Naren, S. Friedemann, G. Zwicknagl, C. Krellner, C. Geibel, F. Steglich, and S. Wirth, Lifshitz transitions and quasiparticle de-renormalization in $YbRh_2Si_2$, New J. Phys. **15**, 093032 (2013).

[64] A. Pourret, S. Sharapov, T. D. Matsuda, G. Knebel, G. Zwicknagl, and A. Varlamov, Transport spectroscopy of the field induced cascade of lifshitz transitions in $YbRh_2Si_2$, J. Phys. Soc. Jpn. **88**, 104702 (2019).

[65] S. Graser, A. F. Kemper, T. A. Maier, H.-P. Cheng, P. J. Hirschfeld, and D. J. Scalapino, Spin fluctuations and superconductivity in a three-dimensional tight-binding model for $BaFe_2As_2$, Phys. Rev. B **81**, 214503 (2010).

[66] G. Zwicknagl and U. Pulst, $CeCu_2Si_2$: Renormalized band structure, quasiparticles and co-operative phenomena, Phys. B (Amsterdam) **186-188**, 895 (1993).

[67] E. K. R. Runge, R. C. Albers, N. E. Christensen, and G. E. Zwicknagl, Electronic structure of $CeRu_2Si_2$, Phys. Rev. B **51**, 10375 (1995).

[68] T. Maehira, T. Hotta, K. Ueda, and A. Hasegawa, Relativistic band-structure calculations for $CeTIn_5$ (T = Ir and Co) and analysis of the energy bands by using tight-binding method, J. Phys. Soc. Jpn. **72**, 854 (2003).

[69] T. Willers, F. Strigari, Z. Hu, V. Sessi, N. Brookes, E. Bauer, J. Sarrao, J. Thompson, A. Tanaka, S. Wirth *et al.*, Correlation between ground state and orbital anisotropy in heavy fermion materials, Proc. Natl. Acad. Sci. USA **112**, 2384 (2015).

[70] E. Bauer, A. Slebarski, E. Freeman, C. Sirvent, and M. Maple, Kondo insulating behaviour in the filled skutterudite compound $CeOs_4Sb_{12}$, J. Phys.: Condens. Matter **13**, 4495 (2001).

[71] M. Maple, P. Ho, V. Zapf, N. Frederick, E. Bauer, W. Yuhasz, F. Woodward, and J. Lynn, Heavy fermion superconductivity in

the filled skutterudite compound $PrOs_4Sb_{12}$, J. Phys. Soc. Jpn. **71**, 23 (2002).

[72] X. Lou, T. L. Yu, Y. H. Song, C. H. P. Wen, W. Z. Wei, A. Leithe-Jasper, Z. F. Ding, L. Shu, S. Kirchner, H. C. Xu, R. Peng, and D. L. Feng, Distinct Kondo screening behaviors in heavy fermion filled skutterudites with $4f^1$ and $4f^2$ configurations, Phys. Rev. Lett. **126**, 136402 (2021).

[73] E. Lengyel, M. E. Macovei, A. Jesche, C. Krellner, C. Geibel, and M. Nicklas, Avoided ferromagnetic quantum critical point in CeRuPO, Phys. Rev. B **91**, 035130 (2015).

[74] M. S. Dresselhaus, G. Dresselhaus, and A. Jorio, *Group Theory: Application to the Physics of Condensed Matter* (Springer, New York, 2007).

[75] M. Tinkham, *Group Theory and Quantum Mechanics* (Dover, New York, 2003).

[76] J. Li, D. Golez, G. Mazza, A. J. Millis, A. Georges, and M. Eckstein, Electromagnetic coupling in tight-binding models for strongly correlated light and matter, Phys. Rev. B **101**, 205140 (2020).

[77] G. Mahan, *Many-Particle Physics* (Springer, New York, 2000).